Ph.D. DISSERTATION

Mutual Interference Mitigation Algorithms for Automotive Radar Systems

차량용 레이더 시스템에서 상호 간섭 신호 완화 기법

BY

KIM JINWOOK

AUGUST 2022

DEPARTMENT OF ELECTRICAL AND
COMPUTER ENGINEERING
COLLEGE OF ENGINEERING
SEOUL NATIONAL UNIVERSITY

Ph.D. DISSERTATION

Mutual Interference Mitigation Algorithms for Automotive Radar Systems

차량용 레이더 시스템에서 상호 간섭 신호 완화 기법

BY

KIM JINWOOK

AUGUST 2022

DEPARTMENT OF ELECTRICAL AND
COMPUTER ENGINEERING
COLLEGE OF ENGINEERING
SEOUL NATIONAL UNIVERSITY

Mutual Interference Mitigation Algorithms for Automotive Radar Systems

차량용 레이더 시스템에서 상호 간섭 신호 완화 기법

지도교수 김 성 철
이 논문을 공학박사 학위논문으로 제출함

2022년 8월

서울대학교 대학원

전기·정보공학부

김 진 욱

김진욱의 공학박사 학위 논문을 인준함

2022년 8월

위 원 장:	조 남 익	(인)
부위원장:	김 성 철	(인)
위 원:	김 남 수	(인)
위 원:	최 정 환	(인)
위 원:	이 성 욱	(인)

Abstract

A recognition of the surrounding environment is important for stable autonomous driving. Various sensors are used to accurately recognize the driving environment of the vehicle. Among them, the radar sensors have advantages that are cost effective and that less affected by the environment. For this reason, various signal processing techniques have been studied to assist autonomous driving, and some functions are implemented on the chips to be attached to vehicles.

The mutual interference of radar can occur when the operating frequencies of two radars overlap. Usually, the interference signal received through a direct path without being reflected by other objects, resulting in strong signal power. The interference signal can increase noise level in the frequency response or create ghost targets, which do not exist. It causes low detection rates and high false alarm rates. This problem could be worse when the number of radar-equipped autonomous vehicles increased. Therefore, in this dissertation, I propose methods for controlling the interference signal generated in the automotive FMCW radar system using the radar.

First, I propose a method for determining whether the interference signal exists in the received signal. Because ghost targets can occur when the interference signal is received, it is necessary to determine whether the interference signal is received before target detection process. In addition, a method for recognizing the type of modulation of the interference signal is proposed. First, an SVM classifier is used for the study and several features are extracted from the time domain signal to train the SVM classifier. Also, I propose a method utilizing the CNN model that takes frequency responses of the received signals as input.

Next, I propose a method for detection of interval in which the interference signal is received. Before canceling the strong interference signal, it is necessary to find the interference interval. The interference interval is detected using the CNN model, and I

confirmed that the performance is higher than previously proposed methods.

Finally, I propose a method for signal reconstruction in the detected interference interval. The detected interference signal is usually replaced with 0 or newly restored. If it is incorrectly generated, artifacts can be generated in the frequency responses. To solve this problem, an approximation of the signal is performed by phase correction of the received signal for the first step. Then, more precise reconstruction is performed using the Doppler frequency of the received signal. With simulated data and measured data, I verified that the proposed method mitigates the interference signal, while suppressing residual frequency responses to be generated.

Contents

List of Tables

List of Figures

Chapter 1

Introduction

These days, interest in stable driving of autonomous vehicles is increasing. Advanced driver assistant system (ADAS) supports lots of functions of autonomous driving. To achieve safe driving condition, the recognition of surrounding environment is essential. Several sensors are used for the recognition, including light detection and ranging (LIDAR), ultrasound, vision, and radio detection and ranging (RADAR) sensors [1]. Among them, radar has advantages because it is relatively least affected by the surrounding environment including bad weather conditions or time of day, and has a relatively longer detection range than the other sensors [2]. For these reasons, radar is widely used as an automotive sensor and is being developed to operate in the 24 GHz and 77 GHz frequency bands [3,4]. The frequency-modulated continuous wave (FMCW) radar is widely used as an automotive radar [5]. Recently, the fast chirp FMCW radar has been used for target estimation on the road [6].

In an automotive radar system, the antenna of a radar-equipped vehicle receives signals reflected from targets, roadside clutter, or structures of iron tunnels. When another radar-equipped vehicle is nearby, undesired signals emitted from that vehicle can be received by the antenna. These signals are defined as interference signals in our work. If the frequency bands of the interference signals overlap with those of the target signals, several pulse-like signals are produced after low-pass filtering. These

signals are distributed in a wide frequency band in the frequency-domain, therefore causing the noise level to increase [7–9]. An increase in signal noise level can make target estimation difficult or even impossible. Moreover, the interference signals can create ghost targets, i.e., mean unwanted and non-existing targets, which may cause false alarms [8, 10]. Furthermore, if the number of radar-equipped vehicles increases in the future, these problems can become more significant.

There are studies on suppressing the interference signals [11–17]. These studies employed several techniques including digital beamforming, signal processing, waveform design and frequency hopping for mitigating the interference signals. Among these interference mitigation fields, I proposed several signal processing methods to deal with the interference signals.

As the first step of signal processing flows for the interference mitigation, I proposed two methods, which can be operated in the time domain and the frequency domain, respectively. Each method identifies the existence of interference signals in the received signals and classifies the types of modulation of signals. In the case of the time-domain algorithm, several features that represent the received signal are extracted from the time-domain signals. The support vector machine (SVM) model is employed for study and the extracted features are used as inputs of the model. Also, I proposed a convolutional neural network (CNN)-based identification and classification method. The method used frequency responses of the received signals to train the network. The performance of two models were analyzed and comparisons with conventional methods were conducted.

Then, the detection of interval where the interference signals received is performed. The signals emitted from other radars are sampled together with the desired target signals. To mitigate the interference signals effectively, the detection of interference interval is performed prior to the mitigation step. I used an CNN model to detect the interference signals in time-domain samples. The detection performance of the CNN model was verified.

Finally, the interference mitigation method is proposed. The detected interference signals were eliminated and I reconstructed the signals using target signals. I recovered the signals using a phase compensation by velocity estimation. Also, I increased the reconstruction performance increased by changing the axis, which the reconstruction is performed.

In Chapter 2, the principle of target estimation in the fast chirp FMCW radar system is discussed. Also, the modulation techniques of five different signals that are used for modeling the interference signals are introduced. Next, mathematical expressions of mixer output signals when the interference signal is received together with the target signal are introduced. Furthermore, the corresponding influences of the interference signals are discussed. In Chapter 3, the proposed identification of interference signal and classification of modulation type methods are introduced. First, the time-domain SVM-based method is analyzed in Section 3.2. An explanation of frequency-domain CNN-based method follows in Section 3.3. In Chapter 4, the interference mitigation techniques are proposed. In Section 4.2, the CNN based interference interval detection method is introduced. Then, interference signal mitigation method is suggested in Section 4.3.

Chapter 2

Automotive FMCW Radar Systems and Interference Signals

2.1 FMCW Radar Systems

I assume that the ego-vehicle transmits fast chirp FMCW radar signals for target detection. The fast chirp FMCW radar has an advantage over the conventional FMCW radar in terms of efficiency of target estimation. In the case of conventional systems, a target pairing process is necessary for target estimation. In multi-target situations, the pairing process can be a time-consuming task. In contrast, in the fast chirp FMCW radar system, the target estimation can be done without the target pairing process because the peaks corresponding to the targets appear in the 2D range-Doppler response [18]. For this reason, the fast chirp FMCW is the most widely used automotive radar system for autonomous driving. Fig. 1 shows this system, in which a transmitting antenna transmits a chirp signal whose frequency increases linearly with time. The transmitter repeatedly sends M chirps and the corresponding transmitted signal can be expressed

as

$$S_{TX}(t, m) = A_T \exp\left(j2\pi\left(\left(f_c - \frac{BW}{2} \right) t + \frac{BW}{2\Delta T}t^2 \right) \right.$$
$$\left. + j\phi_T \right) \qquad (0 \le t < \Delta T,\, 0 \le m < M), \qquad (2.1)$$

where A_T is the amplitude of the transmitted signal, f_c is the carrier frequency of the radar, BW is the bandwidth, ΔT is the sweep time of a chirp, t is the time value in the fast-time axis, m is the chirp index, and ϕ_T is the initial phase of the transmitted signal. A receiver receives these M chirps signals that are reflected from a target. The corresponding phase of the received signal can be expressed as

$$\phi_{RX}(t, m) = \left(f_c - \frac{BW}{2} + f_D \right)(t - t_d) + \frac{BW}{2\Delta T}(t - t_d)^2$$
$$(t_d \le t < \Delta T,\, 0 \le m < M). \qquad (2.2)$$

Compared to (2.1), there are phase differences in (2.2), which are caused by the target motion. The first one is from the Doppler shift f_D, which can be expressed as $\frac{2f_c v}{c}$. This is caused by the relative velocity v between the radar and the target. The second one is from the round-trip delay $t_d = \frac{2R(m)}{c}$, where t_d is the time delay for the transmitted signal to reach the target and return to the receiver and $R(m)$ is the distance between the radar and the target. Here, $R(m)$ is the distance for the mth chirp which can be expressed as $R + mv\Delta T$, where R is the initial range. This is because the radar and the target move with relative velocity v, which causes the range offset from the initial range R.

The received signals are then multiplied with the transmitted signal in a mixer to obtain a signal at the intermediate frequency. Higher frequency components are filtered with the low-pass filter. The corresponding phase of the mixer output signal

can be expressed as

$$
\begin{aligned}
\phi_{MX}(t,\, m) = &-f_D t + f_c t_d - \frac{BW}{2} t_d + f_D t_d \\
&+ \frac{BW}{\Delta T} t t_d - \frac{BW}{2\Delta T} {t_d}^2
\end{aligned}
$$

$$(t_d \le t < \Delta T,\, 0 \le m < M). \tag{2.3}$$

The first, third, fourth, and last terms, which are expressed as $f_D t$, $\frac{BW}{2} t_d$, $f_D t_d$, and $\frac{BW}{2\Delta T} {t_d}^2$, respectively, can be neglected because they are relatively smaller than the other terms. Considering that $f_D = \frac{2 f_c v}{c}$ and $t_d = \frac{2(R + m v \Delta T)}{c}$, $\phi_{MX}(t,\, m)$ can be approximated as

$$
\begin{aligned}
\phi_{MX}(t,\, m) \approx &\frac{2 f_c R}{c} + \frac{2 f_c v \Delta T}{c} m + \frac{2 BW R}{\Delta T c} t \\
&+ \frac{2 BW v m}{c} t
\end{aligned}
$$

$$(t_d \le t < \Delta T,\, 0 \le m < M). \tag{2.4}$$

Again, the last term $\frac{2 BW v m}{c} t$ can be neglected because it is relatively smaller than the other terms. Finally, $\phi_{MX}(t,\, m)$ can be approximated as

$$
\phi_{MX}(t,\, m) \approx \frac{2 f_c R}{c} + \frac{2 f_c v \Delta T}{c} m + \frac{2 BW R}{\Delta T c} t
$$

$$(t_d \le t < \Delta T,\, 0 \le m < M). \tag{2.5}$$

Each chirp signal is sampled by an analog-to-digital converter (ADC) and N is the number of samples in a single chirp. Thus, the mixer output is defined in a $N \times M$ matrix form as

$$
\mathbf{S} = [\boldsymbol{s}_c(1),\ \boldsymbol{s}_c(2),\ \cdots,\ \boldsymbol{s}_c(M)], \tag{2.6}
$$

where $\boldsymbol{s}_c(m) = [s(1,\, m), \cdots, s(N,\, m)]^T$ and $s(n,\, m)$ is defined as

$$
\begin{aligned}
s(n,\, m) = A_M \exp \Bigg(j 2\pi \Bigg(&\frac{2 f_c R}{c} + \frac{2 f_c v}{c} \Delta T m \\
&+ \frac{2 BW R}{\Delta T c} \frac{\Delta T}{N} n \Bigg) + j \phi_s \Bigg).
\end{aligned}
$$

$$\tag{2.7}$$

In (2.7), A_M is the amplitude of the mixer output signal and ϕ_s is the phase offset.

When applying 2D Fourier transform on $\mathbf{S}$ in (2.6), I can estimate the target's velocity and range simultaneously. The resulting frequency response is called the range-Doppler response. The 2D Fourier transform can be performed step by step; for example, a column-wise Fourier transform can be performed first, followed by a row-wise Fourier transform. When column-wise Fourier transform is applied on the signal matrix $\mathbf{S}$, a peak appears at a specific frequency which corresponds to the last term in (2.7), $\frac{2BWR}{\Delta Tc}$. Therefore, this frequency implies the distance between the radar and the target. The corresponding frequency responses can be expressed in a $N_c \times M$ matrix form, where N_c is the number of points in the column-wise Fourier transform, as

$$\mathbf{X}_c = [\boldsymbol{x}_c(1),\ \boldsymbol{x}_c(2),\ \cdots,\boldsymbol{x}_c(M)]\,, \tag{2.8}$$

here $\boldsymbol{x}_c(m) = [x(1,m),\cdots,x(N_c,m)]^T$ and $x(n_c,m)$ is defined as

$$x(n_c,m) = \sum_{n=1}^{N} s(n,m)\exp\left(-j\frac{2\pi n}{N_c}n_c\right). \tag{2.9}$$

(a)   (b)
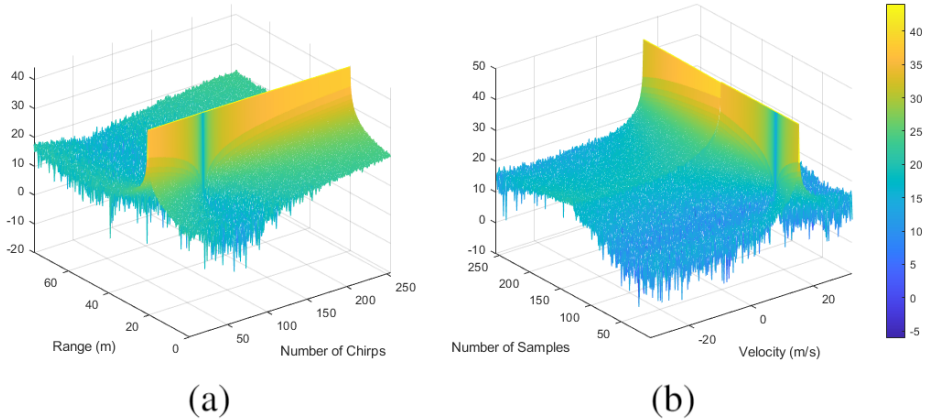
Figure 2.1: Frequency responses of fast chirp FMCW radar system (a) after column-wise Fourier transform (b) after row-wise Fourier transform
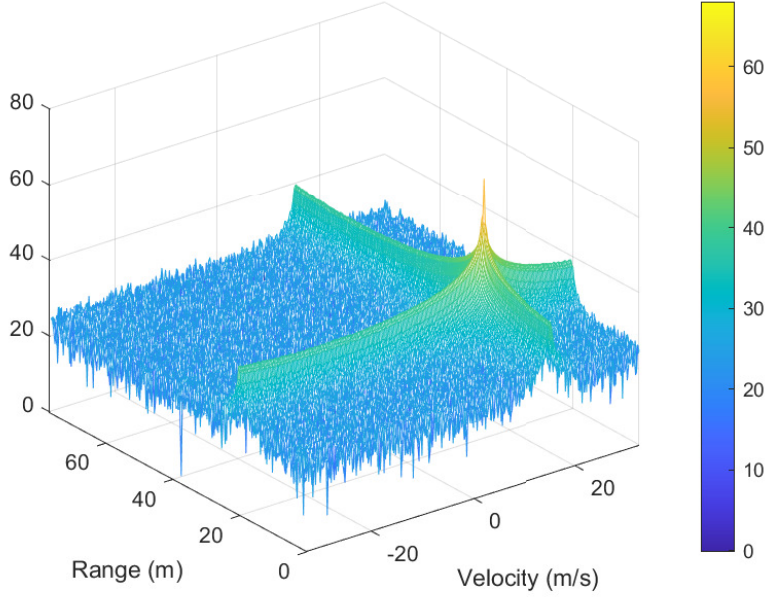
Figure 2.2: Range-Doppler response of fast chirp FMCW radar system: a peak corresponding to target appears at $(R,\ v) = (20\text{ m},\ 15\text{ m/s})$

Here, $\boldsymbol{x}_c(m)$ is the frequency response of $\boldsymbol{s}_c(m)$ and $\mathbf{X}_c$ is the frequency response following the column-wise Fourier transform.

Next, in (2.8), I apply Fourier transform on each row vector $\boldsymbol{x}_{cr}(n_c)$ in $\mathbf{X}_c$, where $\boldsymbol{x}_{cr}(n_c)$ is defined as $\boldsymbol{x}_{cr}(n_c) = [x(n_c, 1), \cdots, x(n_c, M)]$. The range-Doppler response can be expressed in a $N_c \times N_r$ matrix form, where N_r is the number of points in the row-wise Fourier transform, as

$$\mathbf{X}_{rv} = \begin{bmatrix} \boldsymbol{x}_{rv}(1) \\ \boldsymbol{x}_{rv}(2) \\ \vdots \\ \boldsymbol{x}_{rv}(N_c) \end{bmatrix}, \tag{2.10}$$

where $\boldsymbol{x}_{rv}(n_c) = [x_{rv}(n_c, 1), \cdots, x_{rv}(n_c, N_r)]$ is the frequency response of $\boldsymbol{x}_{cr}(n_c)$

and $x_{rv}(n_c, n_r)$ is defined as

$$x_{rv}(n_c, n_r) = \sum_{m=1}^{M} x(n_c, m) \exp\left(-j\frac{2\pi m}{N_r} n_r\right). \qquad (2.11)$$

Fig. 2.1(a) shows the result of the column-wise Fourier transform when a single target moves at a speed of 20 m/s at a distance of 15 m. As shown in the figure, peaks are generated at 15 m in every column. In addition, a relative velocity between radar and target can be obtained when applying Fourier transforms on each row of $\mathbf{S}$. As shown in Fig. 2.1(b), peaks appear at the frequency of $\frac{2f_c v}{c}$, which is the second term in (2.7). Therefore, I can estimate that the target moves at a speed of 15 m/s.

Fig. 2.1 shows a range-Doppler response of the signal received from the target I set above. As shown in the figure, peaks appear at certain values on the range and velocity axis, enabling the estimation of the target information as $R = 20$ m and $v = 15$ m/s. Furthermore, if two or more targets exist, the corresponding peaks appear at the range-Doppler response. Therefore, I can simultaneously estimate both the range and velocity of each target.

2.2 Interference Signals in FMCW Radar Systems

2.2.1 Other types of frequency-modulated signals

There are several modulation techniques for estimating target information [1], and I selected five different modulations to model the incoming interference signals: the unmodulated CW, slow chirp FMCW, fast chirp FMCW, pulsed CW, and frequency-shift keying signals. In this section, each modulation technique is briefly introduced. A description of the fast chirp FMCW signal will be skipped as I have already discussed in Section 2.1.

a

b

c

d
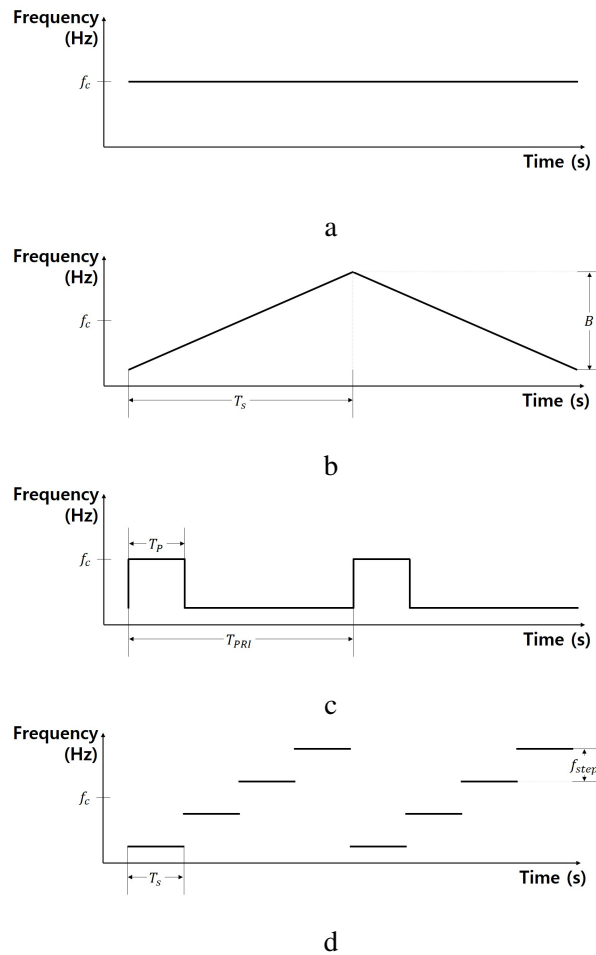
Figure 2.3: Time-frequency graph for four different modulated signals
(a) unmodulated CW, (b) slow chirp FMCW radar system, (c) pulsed CW, and (d)
frequency-shift keying signals

Unmodulated CW Signal

In this modulation, the frequency of the signal is constant during the transmission period, as shown in Fig. 2a. The frequency of an unmodulated CW signal and the corresponding transmitted signal can be expressed as

$$f(t) = f_c \quad (0 \le t < T_{period}), \tag{2.12}$$

$$S_t(t) = A \exp\left(j2\pi f_c t\right), \tag{2.13}$$

where A is the amplitude of the signal, and T_{period} is the signal transmission period. Only the velocity information can be obtained through conjugate mixing [1].

Slow Chirp FMCW Signal

A slow chirp FMCW radar system transmits chirp signals that consist of an up-chirp and a down-chirp, as shown in Fig. 2b. In the up-chirp period, the frequency of the signal increases linearly, and in the down-chirp period, the frequency of the signal decreases linearly. The frequency of a slow chirp FMCW signal and the corresponding transmitted signal can be expressed as

$$f(t) = \left(f_c + (-1)^{n_S} \frac{B}{2}\right) - (-1)^{n_S} \frac{B}{T_s}\left(t - n_S T_s\right),$$
$$n_S = \left\lfloor \frac{t}{T_s} \right\rfloor \quad (0 \le t < T_{period}), \tag{2.14}$$

$$S_t(t) = A \exp\left(j2\pi\left(\left(f_c + (-1)^{n_S} \frac{B}{2}\right.\right.\right.$$
$$\left.\left.\left. + (-1)^{n_S} n_S B\right) t - (-1)^{n_S} \frac{B}{2T_s} t^2\right)\right), \tag{2.15}$$

where n_S represents the index of the chirp and it can be obtained from the floor operator $\lfloor \cdot \rfloor$. The range and the velocity information can be obtained through pairing beat frequencies of mixer outputs of the up-chirp signal and the down-chirp signal [1].

Pulsed CW Signal

A pulsed CW signal transmits periodic pulses, and the duration of each pulse is relatively smaller than the pulse period, as shown in Fig. 2c. The duration is defined as a pulse duration time, T_P, and the pulse period is defined as a pulse repetition interval (PRI), T_{PRI}. The frequency of a pulsed CW signal and the corresponding transmitted signal can be expressed as

$$f(t) = \sum_{n_P=0}^{N_P-1} f_c rect\left(\frac{t - n_P T_{PRI}}{T_P}\right) \quad (0 \le t < T_{period}), \tag{2.16}$$

$$S_t(t) = A \exp\left(j2\pi\left(\sum_{n_P=0}^{N_P-1} f_c rect\left(\frac{t - n_P T_{PRI}}{T_P}\right)t\right)\right), \tag{2.17}$$

where $rect(\cdot)$ is a rectangular function, and N_P is the number of pulses. The range and the velocity information can be obtained through a correlation method [1].

FSK Signal

The frequency of a FSK signal consists of M different frequency steps, and every two adjacent steps have the same frequency difference, as shown in Fig. 2d. The frequency of an FSK signal and the corresponding transmitted signal can be expressed as

$$f(t) = f_c - f_{step}\left(\frac{M - 1 - 2\left(n_F \bmod M\right)}{2}\right),$$

$$n_F = \left\lfloor \frac{t}{T_s} \right\rfloor \quad (0 \le t < T_{period}), \tag{2.18}$$

$$S_t(t) = A \exp\Bigg(j2\pi\bigg(f_c$$

$$-f_{step}\left(\frac{M - 1 - 2\left(n_F \bmod M\right)}{2}\right)\bigg)t\Bigg), \tag{2.19}$$

where n_F represents the index of the pulse, and f_{step} is the difference between two adjacent steps. The range and velocity information can be obtained through the inverse

Fourier transform [1].

2.2.2   Analysis of Time-Domain Mixer Output Signals

In this section, the problems that arise when the desired target signal is received with the interference signals will be discussed. Based on the expressions and analyses of radar modulation techniques, I will investigate the time-domain mixer output signal expressions when various kinds of interference signals exist. Then, the time-domain and the frequency-domain signal graphs will be introduced.
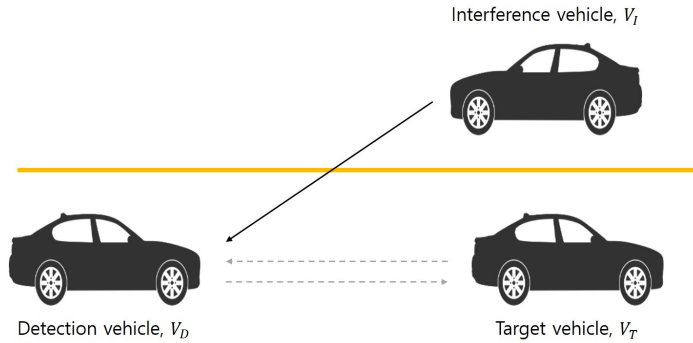
Figure 2.4: Interference system diagram

As shown in Fig. 2.4, three vehicles are set up in our work. A detection vehicle, V_D, that is equipped with a fast chirp FMCW radar, a target vehicle, V_T, that is driving in front of the detection vehicle, and an interference vehicle, V_I, that is driving towards the detection vehicle and is transmitting various types of interference signals.

To investigate the effect of an interference signal, I will check the mixer output signal. In Section 2.1, I multiplied the transmitted fast chirp FMCW signal and the received fast chirp FMCW signal for target estimation, as in (5). However, in the case when an interference signal exists, I replace $S_r(\hat{t})$ in (5) with the signal transmitted from other vehicles that use different modulations. Moreover, rather than constructing a 2D matrix for target estimation, I used a 1D time-domain signal for analyzing the in-

fluence of the interference signals. As shown in Fig. 1, the frequency of the transmitted signal in the fast chirp FMCW system can be expressed as

$$f(t) = \left(f_c - \frac{B}{2} \right) + \frac{B}{T_s} \left(t - nT_s \right), \ n = \left\lfloor \frac{t}{T_s} \right\rfloor. \tag{2.20}$$

The corresponding transmitted signal can be expressed as

$$S_t(t) = \exp\left(j2\pi \left(\left(f_c - \frac{B}{2} - nB \right) t + \frac{B}{2T_s} t^2 \right) \right), \tag{2.21}$$

where the amplitude of the signal is normalised to one for simplicity.

For the five different modulation techniques, each received signal expression, $S_r(t)$, is derived from its corresponding transmitted signal expressions, as in (15), (17), (19), and (21). For the fast chirp FMCW signal, $S_r(t)$ is derived from (23). Like in (4) and (5), $S_r(t)$ is derived from $S_t(t)$ by taking into account the Doppler shift frequency f_D and the round-trip delay t_d. Furthermore, I added a variable, t_{delay}, which represents the mismatched timing in signal transmission. To distinguish parameters of the radar-equipped vehicle's signal and those of the interference signals, I used the subscript I on the parameters of the interference signals. For convenience, I used subscripts for naming modulation types as follows: "UC" for the unmodulated CW, "SC" for the slow chirp FMCW, "FC" for the fast chirp FMCW, "PC" for the pulsed CW, and "FSK" for the frequency-shift keying. The corresponding five mixer output signals of each modulations can be expressed as

$$\begin{aligned} m_{UC}(t) = \exp\bigg(j2\pi \bigg(&\left(f_c - f_{cI} - f_D - \frac{B}{2} - nB \right) t \\ &+ \left(f_cI + f_D \right) \left(t_d + t_{delay} \right) + \frac{B}{2T_s} t^2 \bigg) \bigg), \end{aligned} \tag{2.22}$$

$$
\begin{aligned}
m_{SC}(t) = \exp\bigg(j2\pi \bigg(\bigg(& f_c - f_{cI} - f_D - \frac{B}{2} \\
& + (-1)^{n_S}\frac{B_I}{2} - nB + (-1)^{n_S} n_S B_I + \\
& (-1)^{n_S}\frac{B_I}{T_{sI}}\left(t_d + t_{delay}\right) \bigg) t \\
& + \frac{1}{2}\left(\frac{B}{T_s} - (-1)^{n_S}\frac{B_I}{T_{sI}} \right) t^2 \\
& + \left(f_{cI} + f_D - (-1)^{n_S}\frac{B_I}{2} - (-1)^{n_S} n_S B_I \right) \\
& \left(t_d + t_{delay}\right) \\
& - (-1)^{n_S}\frac{B_I}{2T_{sI}}\left(t_d + t_{delay}\right)^2 \bigg) \bigg),
\end{aligned}
\tag{2.23}
$$

$$
\begin{aligned}
m_{FC}(t) = \exp\bigg(j2\pi \bigg(\bigg(& f_c - f_{cI} - f_D - \frac{B}{2} + \frac{B_I}{2} \\
& - nB + n_I B_I + \frac{B_I}{T_{sI}}\left(t_d + t_{delay}\right) \bigg) t \\
& + \frac{1}{2}\left(\frac{B}{T_s} - \frac{B_I}{T_{sI}} \right) t^2 \\
& + \left(f_{cI} + f_D - \frac{B_I}{2} - n_I B_I \right)\left(t_d + t_{delay}\right) \\
& - \frac{B_I}{2T_{sI}}\left(t_d + t_{delay}\right)^2 \bigg) \bigg),
\end{aligned}
\tag{2.24}
$$

$$
\begin{aligned}
m_{PC}(t) = \exp\bigg(j2\pi \bigg(\bigg(& f_c - \sum_{n_P=0}^{N_P-1} f_{cI}\, rect\left(\frac{t - n_P T_{PRI}}{T_P} \right) \\
& - f_D - \frac{B}{2} - nB \bigg) t + \frac{B}{2T_s} t^2 \\
& + \left(\sum_{n_P=0}^{N_P-1} f_c\, rect\left(\frac{t - n_P T_{PRI}}{T_P} \right) + f_D \right) \\
& \left(t_d + t_{delay}\right) \bigg) \bigg),
\end{aligned}
\tag{2.25}
$$

15

$$m_{FSK}(t) = \exp \left(j2\pi \left(\left(f_c - f_{cI} - f_D - \frac{B}{2} - nB \right. \right. \right.$$

$$\left. + f_{step} \left(\frac{M - 1 - 2\,(n \bmod M)}{2} \right) \right) t$$

$$+ \frac{B}{2T_s} t^2 + \left(f_{cI} + f_D \right.$$

$$\left. - f_{step} \left(\frac{M - 1 - 2\,(n \bmod M)}{2} \right) \right)$$

$$\left. \left. \left. \left(t_d + t_{delay} \right) \right) \right). \tag{2.26}$$

For simplicity, all signal amplitudes are normalised to 1.

The time-domain mixer output signals of the five different modulations are shown in Fig. 4. Each modulation type is shown in the title of figures. In the time-domain signal graphs, the desired target signals are densely distributed in the middle, and the interference signals are sparsely distributed. The amplitudes of the interference signals are usually larger than that of the desired target signal because the interference signals are directly propagated from the interference vehicle to the receiving antenna, whereas the desired target signals are reflected at the target vehicle, causing the signals to be attenuated. The sparsely distributed strong interference signals distort the frequency responses, making it difficult to estimate the target.

2.2.3 Range-Doppler Response of the Interference Signal

In this section, the frequency responses of interference signals are introduced. First, the impact of interference signal is analyzed. When the slopes of two radars are different, the noise floor increases. Fig. 2.7(a) shown the case when three targets are detected. However, when the interference signal received, two peaks are masked due to interference signals as shown in Fig. 2.7(b). On the other hand, when the slopes of two radars are same, the ghost target can be generated. As shown in Fig. 2.8(b), the ghost target is generated when the interference signal received. For these reasons, the interference signals degrade target estimation performance. Therefore, the interference signals should be suppressed for reliable target estimation.

Next, the range-Doppler responses of interference signals according to the modulation types are introduced. As signals from (2.22) to (2.26) are given in the form of a vector with a single time index, they must be converted into a matrix form of size $N \times M$ to check the range-Doppler responses, as shown in (2.6). The NM data samples sampled in the ADC are converted to the matrix form of (2.6), and then the range-Doppler response is obtained through the processes of (2.8)-(2.11). Analyzing the magnitude of range-Doppler responses, as presented in Fig. 5, I observe that different patterns are generated according to the modulation types. Fig. 5(a) and Fig. 5(b)-(f) show the magnitude of range-Doppler responses when only the target exists and when five different types of interference signals are received together, respectively. From the expressions from (2.22) to (2.26), different frequency components of the interference signals create specific patterns in range-Doppler responses. Therefore, I can expect that a deep learning model trained with the magnitude of these frequency responses can ensure the identification of the interference signals.
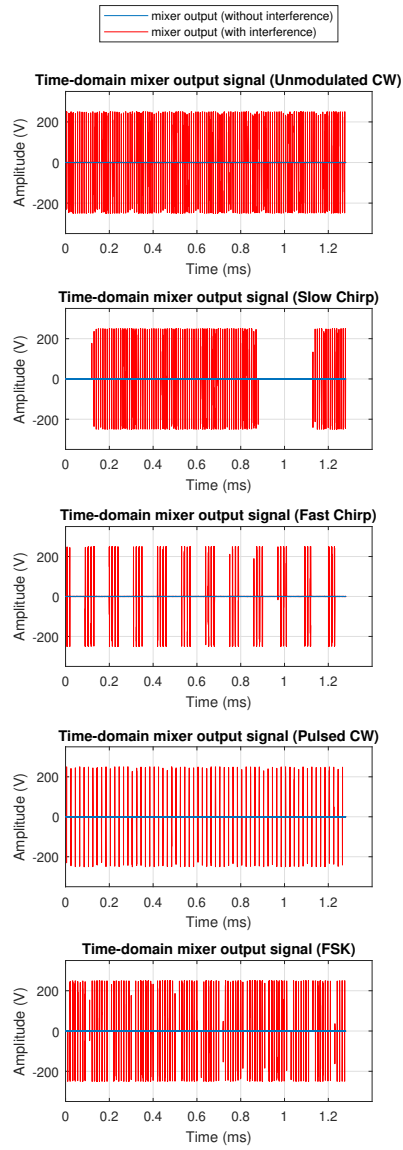
Figure 2.5: Time-domain received signals of five different modulations
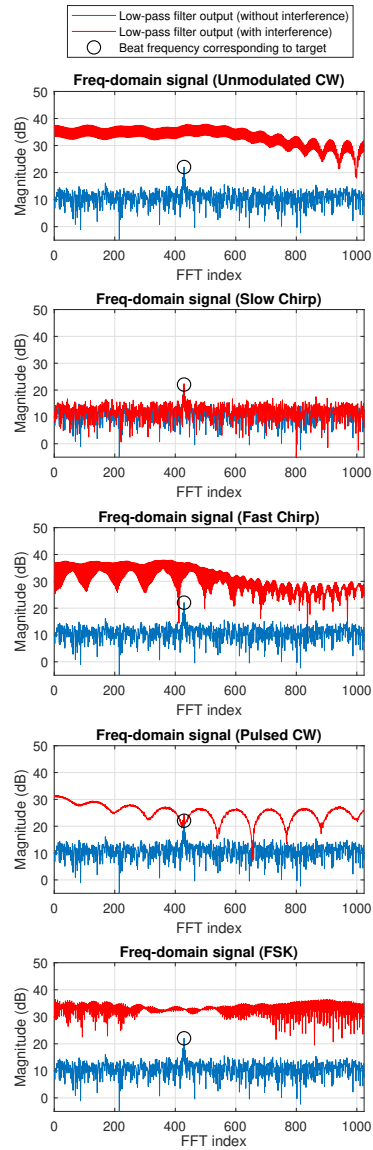
Figure 2.6: Frequency-domain signal of five different modulations
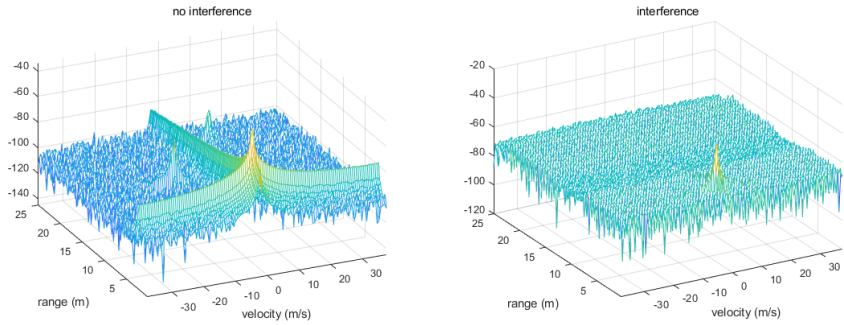
Figure 2.7: Range-Doppler responses when (a) 3 target exist and (b) interference signal received
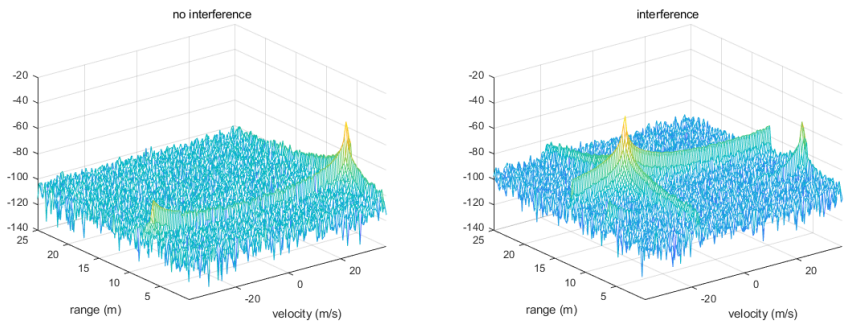
Figure 2.8: Range-Doppler responses when (a) 1 target exists and (b) interference signal received
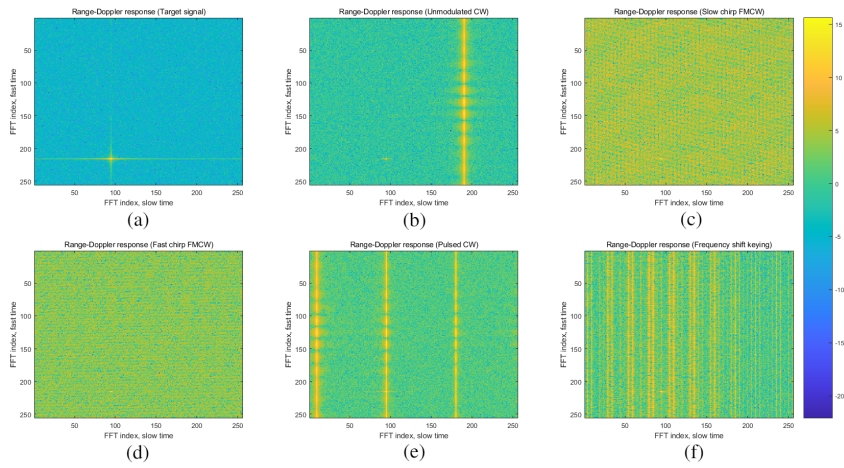
Figure 2.9: Range-Doppler responses of received signals when (a) only target signal, (b) unmodulated CW signal, (c) slow chirp FMCW signal, (d) fast chirp FMCW signal, (e) pulsed CW signal, and (f) FSK signal received

21

Chapter 3

Identification of Existence of Interference Signal and Classification of Modulation of Interference Signal

3.1 Motivation

For the first step of interference handling, the identification of the existence of interference signal is processed. If the identified received signal is the desired target signal, I can decide to perform a target estimation process. Otherwise, I can decide to suppress the interference portion of the signal according to the modulation type of the signal, as I have classified it. A few studies have suggested methods for the identification of interference signals [19], [20]. In [19], a method for identifying the modulation type of interference signals is proposed. The authors used a Gini's coefficient, which represents the inequality of the observation values of the power spectral density of the received signal, as a feature to classify the interference signals. However, the authors assumed that the target signals were not reflected from the target, and did not consider the case where an interference signal and the target signal are received together. This assumption does not reflect driving conditions on the road. In [20], the authors considered the case where a signal of the ego-radar system was received together with a signal of another radar. They suggested a classification model using a support vector

machine (SVM). The frequency responses of received signals were used as input data for the model. They used the entire frequency-domain interference signals and sliced it to make training sets, rather extract features from the frequency responses. Therefore, the complexity of learning and classification process was probably high.

In this chapter, I propose an identification and classification method in both the time domain and the frequency domain. I classified 5 modulation type of interference signal as listed in 2.2. For the time-domain interference classification method, five features, i.e., the mean, variance, skewness, kurtosis, and peak-to-averaged power ratio (PAPR), are extracted from the time-domain mixer output signal. First, I identify whether an interference signal exists or not. If the received signal is verified as the interference signal, then the classification is performed, and the signal is classified according to modulation type. The SVM is used for training and validation. As I extract features from the time-domain signals, rather than using the entire dataset, I expect that this method has an advantage in computational load.

Next, I suggest the interference identification and classification method performed in frequency domain. In the fast chirp FMCW radar system, mutual interference can be effectively analyzed in two axes of slow-time and fast-time, which can be regarded as two-dimensional (2D) data. These 2D data, radar signals with interference, were transformed into a range-Doppler response by utilizing 2D Fourier transform. Thus, I propose a model using a convolutional neural network (CNN) which is effective for the 2D radar data. Recently, CNN's have been actively used in combinations with radar sensor data to classify target types [21–23] or specific actions [21, 24]. In this chapter, I proposed a CNN model composed of convolutional layers, fully connected layers, and an output layer, considering batch normalization and max pooling for better performance.

In simulation results, the proposed CNN-based method can classify five different interference signals with an accuracy of over 96% and it shows better classification accuracy than SVM's used in [20], [25]. Unlike feature-based machine learning tech-

niques, our proposed method does not require hand-crafted features based on domain knowledge. In addition, whereas the conventional method requires the entire chirp data for classification, the proposed method allows classification using only a few chirps. This is to make faster decisions by lowering the amount of computation in generating input data of the CNN model. I took chirp data from the first column and transformed it into 2D range-Doppler response. The proposed algorithm showed 96.5% accuracy even when only 1% of the total chirps were used. I verified that the accuracy increased as the number of chirps used increased.

The remainder of this chapter is organized as follows. In Section 3.2, the proposed time-domain classification algorithm using SVM is introduced. First, the simulation environment is introduced in Section 3.2.1. Then, features that I used in this study is explained in Section 3.2.2. In Section 3.2.3, the classification model using SVM is proposed. Finally, the classification results are analyzed in Section 3.2.4. In section 3.3, the proposed CNN-based classification method is presented. From Section 3.3 to Section 3.3.3, the input type and the framework for the CNN are introduced. The simulation environment is described in Section 3.3.4. Then, the classification results using the CNN are given in Section 3.3.5. Additionally, I also compare the performance of the proposed method to other classification methods. Finally, I conclude this chapter in Section 3.4.

3.2 Time-domain Classification Algorithm with Support Vector Machine

3.2.1 Simulation Environment

To verify the performance of the proposed method, I consider the worst possible situation and consider the case where the interference signal's bandwidth overlaps with a lot of frequency bands of the detection vehicle. If the frequency bands of the signals are overlapped, several interference signals remain after passing the signal through a

mixer. In this case, the interference signal's effect will be significant even after the mixer output signal has passed through an LPF. I set the parameters, including the sweep time and pulse duration, to satisfy the requirements in 77/79 GHz automotive radar systems [26] and [27]. Our main focus was to satisfy the range resolution and velocity resolution conditions. Accordingly, the radar parameters are set as shown in Table 3.1.

Table 3.1: Modulation types of interference signals and mixer output signals

Modulation	Fast chirp FMCW of V_D	Unmodulated CW	Slow chirp FMCW	Fast chirp FMCW of V_I	Pulsed CW	Frequency-shift keying
centre frequency, GHz	76.5	76.5	76.5	76.5	76.5	76.5
bandwidth, MHz	500	—	700	800	—	600
sweep time, μs	10	—	1000	11	—	—
number of samples per chirp	512	—	—	—	—	—
sampling frequency, MHz	51.2	—	—	—	—	—
number of chirp	128	—	—	—	—	—
pulse duration, μs	—	—	—	—	5	—
PRI, μs	—	—	—	—	15	—
step number	—	—	—	—	—	17
frequency step, MHz	—	—	—	—	—	37.5
step duration time, μs	—	—	—	—	—	6

When creating the signals, I considered a wide range of conditions to take into account the diversity of driving environments. Considering the maximum detection range R_{max} in (10) and radar parameters of Table 1, the maximum detection range is $76.8\,\mathrm{m}$. Therefore, I set the range between the detection vehicle and target vehicle, R_t, and the range between the detection vehicle and interference vehicle, R_I, as values from 10 to $70\,\mathrm{m}$. Furthermore, from (11), the maximum unambiguous velocity can be calculated as $98.04\,\mathrm{m/s}$, and I can suppose that the velocity of each vehicle can vary from 0 to $30\,\mathrm{m/s}$. Therefore, the relative velocity between the detection vehicle and the target vehicle varies from -30 to $30\,\mathrm{m/s}$. Furthermore, the relative velocity between the detection vehicle and interference vehicle varies from -60 to $0\,\mathrm{m/s}$. Also, I set t_{delay}, which is the difference in transmission timing between the detection vehicle and the interference vehicle, as a value from 0 to the sweep time T_s.

3.2.2 Class Selection and Feature Selection

To classify the modulation techniques, I used MATLAB and created mixer output signals. I considered five different modulations: unmodulated CW, slow chirp FMCW, fast chirp FMCW, pulsed CW, and FSK. To verify that I could identify the existence of an interference signal, I also created a signal in which only the desired target signal existed. For convenience, I named this non-interference signal as "NI".

Furthermore, I selected the mean, variance, skewness, and kurtosis of the time-domain signal as features when training and validating the SVM. These four features are widely used when the classification uses signals from targets [28]. I also used PAPR, which indicates the ratio of the peak power level to the time-averaged power level. These five features are defined as follows.

Table 3.2: Averaged feature values

Modulation	Feature				
	Mean [V]	Variance [V^2]	Skewness	Kurtosis	PAPR
unmodulated CW	8.90×10^{-3}	2.07×10^{3}	2.05×10^{-3}	2.03×10^{1}	1.45×10^{1}
slow chirp FMCW	8.74×10^{-3}	1.37×10^{3}	9.95×10^{-4}	3.04×10^{1}	2.17×10^{1}
fast chirp FMCW	-8.38×10^{-4}	1.31×10^{3}	-6.22×10^{-3}	3.18×10^{1}	2.27×10^{1}
pulsed CW	-1.84×10^{-3}	5.09×10^{2}	-1.03×10^{-2}	8.04×10^{1}	5.76×10^{1}
frequency-shift keying	-2.80×10^{-1}	1.63×10^{6}	-2.60×10^{-3}	2.57×10^{1}	1.84×10^{1}
non-interference	3.55×10^{-5}	1.26×10^{0}	5.43×10^{-5}	2.69×10^{0}	9.51×10^{0}

$$\mu = \frac{1}{N_f} \sum_{n=1}^{N_f} \Re\left(m(n)\right),$$

$$\sigma = \frac{1}{N_f - 1} \sum_{n=1}^{N_f} \left(\Re\left(m(n)\right) - \mu\right)^2,$$

$$\gamma = \frac{\frac{1}{N_f} \sum_{n=1}^{N_f} \left(\Re\left(m(n)\right) - \mu\right)^3}{\left[\sqrt{\frac{1}{N_f} \sum_{n=1}^{N_f} \left(\Re\left(m(n)\right) - \mu\right)^2}\right]^3},$$

$$k = \frac{\frac{1}{N_f} \sum_{n=1}^{N_f} \left(\Re\left(m(n)\right) - \mu\right)^4}{\left[\frac{1}{N_f} \sum_{n=1}^{N_f} \left(\Re\left(m(n)\right) - \mu\right)^2\right]^2},$$

$$p = \frac{\max_n \left[m(n)m^*(n)\right]}{\frac{1}{N_f} \sum_{n=1}^{N_f} m(n)m^*(n)}, \tag{3.1}$$

where $\Re(\cdot)$ is an operator that takes real parts of the complex signals, $m(n)$ is a discrete-time mixer output signal, and N_f is the number of samples of $m(n)$. The parameters μ, σ, γ, k and p stand for mean, variance, skewness, kurtosis and PAPR, respectively.

For each modulation, I made $1,000$ mixer output signals, and for each modeled signal, I extracted the five features above. Therefore, the dataset consisted of $6 \times 1,000 \times 5$ values. The average values of each feature according to modulation type are shown in Table 3.2.

The scatter plots of feature values that were extracted from interference signals are shown in Fig. 3.1. In Fig. 3.1(a), I can see that the values of the "NI" class are distributed like a line in the 3D scatter plot graph. To show the feature distribution in

detail, a 2D scatter plot with kurtosis and PAPR is shown in Fig. 3.1(b). Most of the feature values of each classes are distributed in certain ares respectively, and some values are distributed along the curved line. Although some values from different classes overlap, I can expect to classify the types of modulation used with classification methods.

3.2.3 Classification using Support Vector Machine

An SVM is an effective classifier for dividing data into two classes and is widely used for classification in several academic fields. In automotive radar applications, the SVM is used for target classification [29]. A linear SVM finds an optimal hyperplane and the corresponding support vectors that maximize the margin between the hyperplane and the data closest to the hyperplane [30]. The linear SVM can be extended to cases that have non-linear boundaries between classes by exploiting kernel functions [31]. The kernel functions include the Gaussian kernel, quadratic kernel and cubic kernel. These kernels transform the original data space into a new data space, which can enable much more effective classifications. As shown in Fig. 3.1(b), the 2D scatter plot has curved lines; therefore, I selected a classifier that was more complicated than the linear SVM. I used the quadratic kernel function for the classification. Also, a binary classification in SVM can be extended to a multi-class classification with the one-against-all method, one-against-one method, and directed acyclic graph SVM (DAGSVM) method [32]. I used the one-against-one method for our classification.

In automotive radar systems, the hardware has limited resources when it comes to computating data. Therefore, it is hard to use algorithms with high computational loads in automotive radar systems. For classifying tasks in automotive systems, I compared the SVM and other classification algorithms, artificial neural network (ANN), in several aspects. First, I analyzed the computational complexity of SVM and recurrent neural network (RNN), which is one of the ANN models and widely used for training sequential data. The computational complexity of SVM is between $O(n^2)$ and $O(n^3)$,
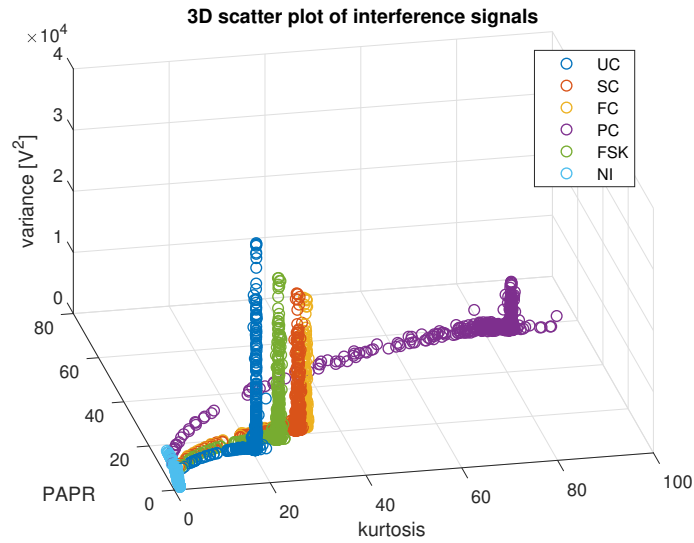
(a)
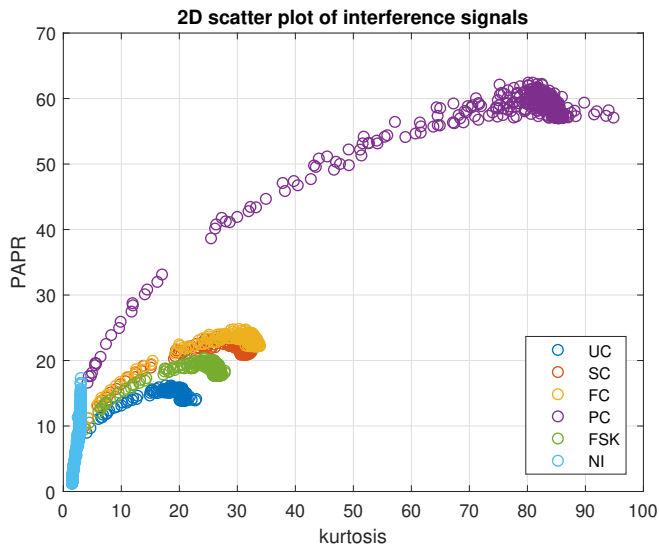
(b)

Figure 3.1: Scatter plots

(a) a 3D scatter plot of a six-class classification with three suggested features, and (b) a 2D scatter plot of a five-class classification with kurtosis and PAPR

where n is the number of training instances [33]. On the other hand, the complexity of RNN is $O(N^2 L)$ per epoch, where N is the number of units in a RNN layer and L is the total number of time steps [34]. Because these two learning methods' complexities are expressed with different parameters, I cannot strictly conclude which method is more complex. Second, a unique global minimum solution is guaranteed when I use SVM, because I can formulate a convex optimization problem. However, when I use ANN, one of the several local minimum solutions may be obtained. Additionally, the SVM is less prone to overfitting than ANN [35]. Overfitting is a tendency to learn unwanted portions of data such as noise. Because it degrades the performance of models, I thus have to consider several techniques to avoid overfitting. However, the SVM is quite resistant to overfitting. Therefore, as the SVM has several advantages over ANN, I selected the SVM for classifying the interference signals.

I verified the performance of the classification from a 5-fold cross-validation. I randomly divided the entire dataset into five groups, and trained a classification model with four groups. Then, I validated the trained model with the remaining one group. The classification accuracy was averaged after performing classifications with four different combinations of divided groups.

3.2.4 Classification Results

First, I verified the identification performance of whether the interference signals exist or not. The interference signals of five different modulations, "UC", "SC", "FC", "PC", and "FSK" were grouped into the 'INT' class, which stands for interference. Therefore, the dataset consisted of 5000 samples of the "INT" class and 1000 samples of the "NI" class. The confusion matrix of the two-class classification is shown in Table 3.3. Each row of the confusion matrix corresponds to a predicted class, and each column corresponds to a true class. As shown in Table 3.3, the accuracy of identification was calculated as over 99.8%. Therefore, I can say that, if the interference signals are received with the target signal, I can notice it and decide to apply interference

suppression techniques.

Table 3.3: Confusion matrix for the identification of presence of interference signals using SVM

True class/predicted class	Interference, %	Non-interference, %
interference	99.8	0.2
non-interference	0	100

After identifying the presence of the interference signals, I classified the interference signals into five classes: "UC", "SC", "FC", "PC", and "FSK". Each class has 1000 samples of data, therefore the dataset consists of 5000 samples. The resulting confusion matrix is shown in Table 3.4, and the accuracy of classification is over 96%. Furthermore, the averaged accuracy of classification is calculated as 98.6%. Although the classification accuracies of class "SC" and "FC" are slightly lower than those of the other classes, the majority of the samples are classified well. I can conclude that five features of time-domain mixer output signals are appropriate for the identification of the presence of the interference signals and the classification of the modulation types of the interference signals.

Table 3.4: Confusion matrix for the classification of interference signals using SVM

True class/predicted class	Unmodulated CW, %	Slow chirp FMCW, %	Fast chirp FMCW, %	Pulsed CW, %	Frequency-shift keying, %
unmodulated CW	99.9	0.1	0	0	0.1
slow chirp FMCW	0	97.4	3.2	0	0.1
fast chirp FMCW	0	2.4	96.7	1.0	0
pulsed CW	0	0	0	99.0	0
frequency-shift keying	0.1	0.1	0.1	0	99.8

I compared the classification performance with another classification method, the decision tree method. To predict input samples, binary decisions are made from a root node down to a leaf node. Every leaf nodes represent one of the classes [36]. The classification using the decision tree is shown in Table 3.5. The averaged accuracy of classification was calculated as 93.2%, however, when compared to Table 3.4, the accuracy of the decision tree method was lower than that of quadratic SVM.

Table 3.5: Confusion matrix for the classification of interference signals using decision tree method

True class/predicted class	Unmodulated CW, %	Slow chirp FMCW, %	Fast chirp FMCW, %	Pulsed CW, %	Frequency-shift keying, %
unmodulated CW	**96.3**	1.7	1.1	0.5	2.0
slow chirp FMCW	0.2	**88.9**	6.2	0.3	1.7
fast chirp FMCW	1.2	5.6	**89.2**	0.9	2.3
pulsed CW	0.1	0.4	0.8	**97.8**	0.2
frequency-shift keying	2.2	3.4	2.7	0.5	**93.8**

I investigated which features are critical for classification. First, I used only one feature for classification and the result is shown in Table 3.6. The table shows the accuracy of the classification that each class is classified into its class when I change the feature used. I identified that PAPR was the most important feature of the classification, and it is followed in importance by kurtosis, variance, mean and skewness. Then, I have conducted classifications with increasing the number of features used in order of importance of the verified features, and the result is shown in Table 3.7. From Tables. 3.6 and Table 3.7, I verified that the skewness is the least important factor for classification. Therefore, when I need to reduce the complexity of calculation for SVM, I can choose the rest of the four features for classification.

Table 3.6: Classification accuracy when using one feature

(True class, predicted class)/feature	μ, %	σ, %	γ, %	k, %	p, %
(unmodulated CW, unmodulated CW)	2.6	20.0	20.4	99.0	99.9
(slow chirp FMCW, slow chirp FMCW)	47.0	22.9	23.4	40.6	0
(fast chirp FMCW, fast chirp FMCW)	14.4	19.2	41.6	55.7	78.6
(pulsed CW, pulsed CW)	19.5	39.1	0	92.3	97.6
(frequency-shift keying, frequency-shift keying)	20.5	3.2	8.8	20.1	91.5
averaged accuracy	20.8	20.9	18.8	61.5	73.5

Table 3.7: Classification accuracy when increasing the number of features used

(True class, predicted class)/feature	p, %	p, k, %	p, k, σ, %	p, k, σ, μ, %	$p, k, \sigma, \mu, \gamma$, %
(unmodulated CW, unmodulated CW)	99.9	99.7	99.9	99.9	99.9
(slow chirp FMCW, slow chirp FMCW)	0	61.0	79.5	92.1	97.4
(fast chirp FMCW, fast chirp FMCW)	78.6	52.3	91.3	99.9	96.7
(pulsed CW, pulsed CW)	97.6	98.2	99.7	99.4	99.0
(frequency-shift keying, frequency-shift keying)	91.5	99.7	99.8	99.8	99.8
averaged accuracy	73.5	82.2	94.0	98.2	98.6

I compared the classification performance of our work with that of [20]. Frequency-domain signals were obtained by applying Fourier transform on the time-domain mixer output signals. I divided the frequency-domain signals in order to make a training

dataset and trained the data with linear SVM as the authors did. The results are shown in Table 3.8. The table shows the classification accuracies of our work and [20]. The right four columns correspond to the accuracies of [20] and each column represents the number of features used in SVM training. As shown in Table 3.8, classification accuracy improved as the number of used features increased. The method of [20] shows better performance when classifying class "PC", as the accuracy is 100% in every case. However, even when the entire set of features are used for classification, the classification accuracy is lower than our work's accuracy.

Table 3.8: Classification accuracy of proposed method and method of [20]

(True class, predicted class)/method	Proposed, %	128 features, %	256 features, %	384 features, %	512 features, %
(unmodulated CW, unmodulated CW)	99.9	89.7	91.8	91.7	91.9
(slow chirp FMCW, slow chirp FMCW)	97.4	30.3	47.1	57.0	64.9
(fast chirp FMCW, fast chirp FMCW)	96.7	40.2	50.7	57.9	61.1
(pulsed CW, pulsed CW)	99.0	100.0	100.0	100.0	100.0
(frequency-shift keying, frequency-shift keying)	99.8	86.1	90.7	92.7	92.8
averaged accuracy	98.6	69.3	76.1	79.9	82.1

3.3 Frequency-domain Classification Algorithm with Convolutional Neural Network

3.3.1 Input Format

To classify the modulation types of interference signals, I consider a CNN model. Compared to an artificial neural network, the CNN employed convolution operations for learning, resulting a reduction in the number of training parameters and effective extraction of the local characteristics of the input image [37].

For the classification task, I use the magnitudes of range-Doppler responses $\mathbf{X}_{rv}$. First, these magnitudes are normalized to values from 0 to 1. When the maximum and minimum values of $x_{rv}(n_c, n_r)$ in all data set are x_{rv}^{max} and x_{rv}^{min}, respectively, the normalized value $x_{rv}^{norm}(n_c, n_r)$ can be expressed as

$$x_{rv}^{norm}(n_c, n_r) = \frac{x_{rv}(n_c, n_r) - x_{rv}^{min}}{x_{rv}^{max} - x_{rv}^{min}}. \tag{17}$$

Thus, the normalized range-Doppler magnitude responses are defined in a matrix form as $\mathbf{X}_k^{in}$, where k is the index for the modulations of interference signals and the size of $\mathbf{X}_k^{in}$ is $N_c \times N_r$. I use $\mathbf{X}_k^{in}$ as the input of the CNN model for the interference classification. In this study, I set the number of points in the Fourier transforms equal to the number of time-domain data. Therefore, the size of the received signal matrix in the time-domain remains the same after 2D Fourier transform.
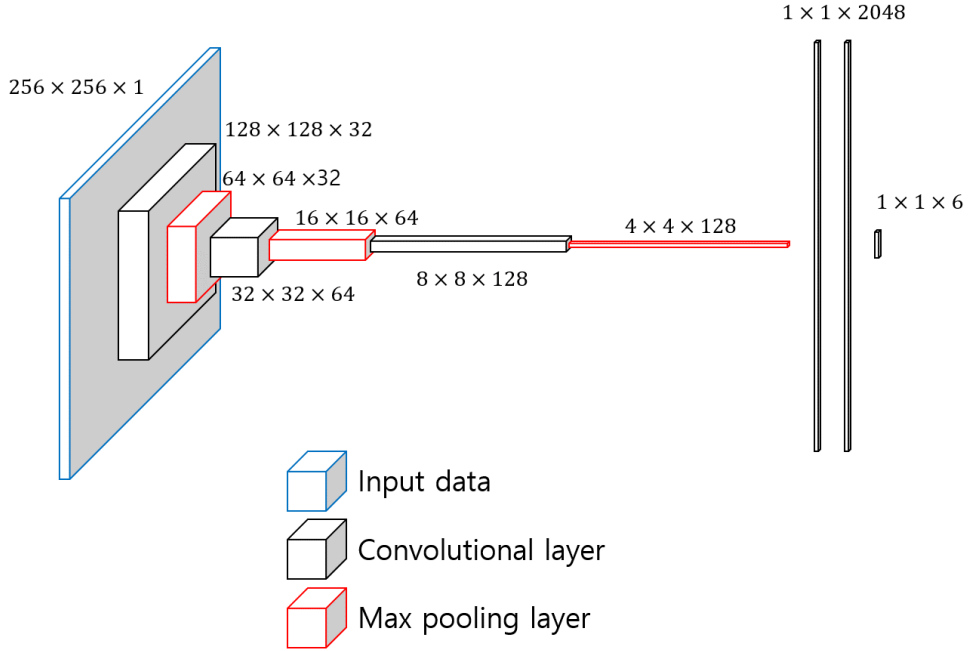
Figure 3.2: The structure of the proposed CNN model

34

Table 3.9: The detailed description of CNN model

Layer	Size of Feature Map	Size of Filters
Input image	$256 \times 256 \times 1$	
Conv	$128 \times 128 \times 32$	$5 \times 5 \times 32$
Batch norm	$128 \times 128 \times 32$	
ReLU activation	$128 \times 128 \times 32$	
Max pooling	$64 \times 64 \times 32$	2×2
Conv	$32 \times 32 \times 64$	$5 \times 5 \times 64$
Batch norm	$32 \times 32 \times 64$	
ReLU activation	$32 \times 32 \times 64$	
Max pooling	$16 \times 16 \times 64$	2×2
Conv	$8 \times 8 \times 128$	$5 \times 5 \times 128$
Batch norm	$8 \times 8 \times 128$	
ReLU activation	$8 \times 8 \times 128$	
Max pooling	$4 \times 4 \times 128$	2×2
Fully connected	$1 \times 1 \times 2048$	
Dropout	$1 \times 1 \times 2048$	
ReLU activation	$1 \times 1 \times 2048$	
Fully connected	$1 \times 1 \times 2048$	
Dropout	$1 \times 1 \times 2048$	
ReLU activation	$1 \times 1 \times 2048$	
Fully connected	$1 \times 1 \times 6$	
Softmax	$1 \times 1 \times 6$	
Output	$1 \times 1 \times 6$	

3.3.2 CNN model

Fig. 3.3.1 shows the structure of our CNN model, which consists of a combination of convolutional layers, batch normalization layers, rectified linear unit (ReLU) activation layers, max pooling layers, fully connected layers, dropout layers, and an output layer. The detailed description of each layer is listed in Table 3.9. Each convolutional layer performs 5×5 convolution operations, and the number of filters increases as the layer becomes deeper. Both the stride and padding size are set to 2 in each convolutional layer. After convolution, the batch normalization is used to normalize the intermediate results of the model. With the batch normalization, the training speed can be improved because a gradient vanishing or gradient exploding can be prevented [38]. Then, I use the ReLU activation function [39], which is defined as

$$f(z^l) = \max\{0, z^l\} = \begin{cases} z^l, & z^l \geq 0 \\ 0, & \text{else} \end{cases} \tag{18}$$

where z^l is an element of outputs in lth convolutional layer. The max pooling layer is used to decrease the spatial size of features and parameters of the network [40]. The units in the final max pooling layer are flattened into a single vector. This final max pooling layer is followed by fully connected layers. Dropout layers are used after each fully connected layer to prevent overfitting [41]. At the output layer, the output for K classes is obtained using a softmax activation function, as follows:

$$\mathbf{z} = [z_1, \cdots, z_K]^T = \sigma(\mathbf{h}), \tag{19}$$

where z_k is the predicted interference representing the kth category in the K classes, $\mathbf{h} = [h_1, \cdots, h_K]^T$ is the output of the last fully connected layer, and $\sigma(\mathbf{h})$ is the softmax function, which is defined as

$$z_k = [\sigma(\mathbf{h})]_k = \frac{e^{h_k}}{\sum_{i=1}^{K} e^{h_i}}. \tag{20}$$

The mini batch size is set to 256, the learning rate is set to 10^{-4}, and the epoch is set to 10 for training.

Table 3.10: Parameter setting of simulation

Modulation type		Parameter	Value
Ego-vehicle	Fast chirp FMCW	Center frequency	76.5 GHz
		Bandwidth	500 MHz
		Sweep time	10 μs
		# of samples	256
		Sampling frequency	25.6 MHz
		# of chirps	256
Interference vehicle	Unmodulated CW	Center frequency	76.5 GHz
	Slow chirp FMCW	Center frequency	76.5 GHz
		Bandwidth	700 MHz
		Sweep time	1 ms
	Fast chirp FMCW	Center frequency	76.5 GHz
		Bandwidth	800 MHz
		Sweep time	11 μs
	Pulsed CW	Center frequency	76.5 GHz
		Pulse duration	5 μs
		Pulse repitition time	15 μs
	FSK	Center frequency	76.5 GHz
		Bandwidth	600 MHz
		# of steps	17
		Frequency step	37.5 MHz
		Step duration	6 μs

3.3.3 Network Optimization

The parameters for the CNN model are learned through training dataset $\mathcal{T}$ to minimize the loss function. Based on the cross-entropy, the loss function for the jth training sample is calculated as

$$Loss(\mathbf{z}^{(j)}) = -\sum_{k=1}^{K} t_k^{(j)} \log(z_k^{(j)}), \tag{21}$$

where $t_k^{(j)} = 1$ when k is the index for the ground truth of the jth training sample and $t_k^{(j)} = 0$ otherwise. The total loss for the training set is calculated as

$$\mathcal{J}(\Theta) = \frac{1}{|\mathcal{T}|} \sum_{j \in \mathcal{T}} Loss(\mathbf{z}^{(j)}), \tag{22}$$

where Θ represents all learnable parameters for the CNN model and $|\cdot|$ is the number of elements in a set.

To minimize the loss function, several variants of the gradient-descent method have been studied in the literature, such as AdaGrad, AdaDelta, Adam, and momentum [42]. These optimizers adaptively change the learning rate to properly minimize the loss function. Here, I used the momentum optimizer in our experiments.

3.3.4 Simulation Environment

I evaluated the performance of the proposed method through simulation. As mentioned in Section 2.2.2, the ego-vehicle transmits radar signals to detect the target vehicle in front. The interference vehicle drives in the opposite lane and transmits the interference signals. The distance between the detection and target vehicles varied from 10 m to 70 m. The distance between the detection and interference vehicles was also set to vary from 10 m to 70 m. The range of the relative velocity between the detection and target vehicles was set to vary from -30 m/s to 30 m/s. In the case of relative velocity between the detection and interference vehicles, the velocity was set from -60 m/s to 0 m/s.

The parameters of the detection and interference vehicles are presented in Table 3.10. These system parameters are determined to meet the radar specifications that

vary depending on the environment in which the radar is used. For example, the maximum detectable range is expressed as $\frac{cN}{4BW}$ and the velocity resolution is expressed as $\frac{c}{2f_c M \Delta T}$. The values of N and M are usually determined as a power of 2 with a value ranging from 128 to 512, which are set to 256 in this paper.

I set $K = 6$ classes for classification: one class for the case when only the target signal was received and five classes for the five different modulations. For convenience, I set each class name as follows: "TS" for target signal, "UC" for unmodulated CW radar signal, "SC" for slow chirp FMCW radar signal, "FC" for fast chirp FMCW radar signal, "PC" for pulsed CW radar signal, and "FSK" for FSK radar signal. I generated 10,000 received signals per class and transformed them into $\mathbf{X}_k^{in}$. 70% of the data was used for training, 15% was used for validation, and 15% was used for test. There are several causes of noise in the radar systems, but the most dominant noise is the thermal noise generated by the radar antenna [19]. Thus, to model the noise of the signal, I assumed the noise to be additive white Gaussian noise (awgn) and set signal-to-noise ratio to 10 dB.

In addition, as all signal post-processing should be performed within a signal period of several tens of milliseconds, an efficient and fast signal processing algorithm is required [43]. Therefore, I also trained the CNN model using a small amount of data to reduce the amount of computation. The conceptual diagram is shown in Fig. 7. I selected chirps to be used from the first column of the time-domain signal matrix $\mathbf{S}$. At this time, if the chirp is taken less, the computational operations in the conversion to 2D range-Doppler response get reduced. I analyzed the accuracy of the model by reducing the number of chirps used and attached the corresponding results.

3.3.5 Classification Results

I first verified the performance of the CNN model by varying the number of chirps used. The horizontal axis of Fig. 8 represents the number of chirps used for classification. With the proposed method, I can classify the modulation of interference signal
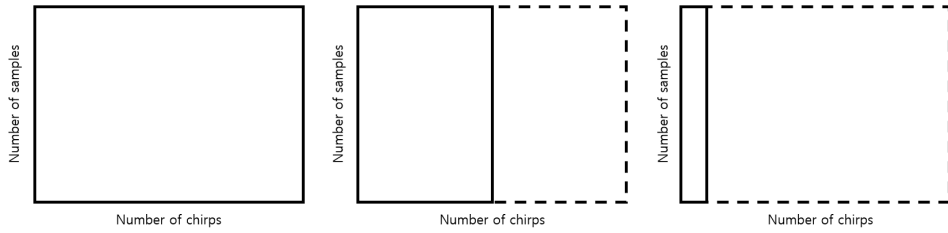
Figure 3.3: Concept diagram showing the use of a small number of chirps

with an accuracy over 96%. The use of only 1% of data for the algorithm enables the classification by the CNN model with an accuracy of 96.8%. This is because even if the number of chirps used is reduced, the characteristics of the signal can be seen in the frequency-domain. Therefore, considering a saving of data storage and fast decision, the task can be performed with considerably less chirps. However, for the selection of the number of chirps used, there is a trade-off between the computational cost and the classification accuracy. Using less chirps results in poor performance because the characteristics in frequency-domain get lost. As the number of chirps used increases, the frequency characteristics become more obvious, so the performance increases. When using 8% of the total data (20 chirps), the performance converges to 100%, which can be interpreted as sufficient to represent the frequency characteristics of the interference signal. Therefore, I can conclude that it is better to use at least 8% of the data to ensure classification performance. Less chirps may be used depending on the purpose.

A training progress when using 20 chirps is shown in Fig. 9. The training accuracy, validation accuracy, training loss and validation loss over epoch number are plotted. As the learning progressed, the accuracy increased and the loss decreased. Finally, the training accuracy and the validation accuracy converged to 100%. Also, because the training loss and the validation loss showed similar tendency, I can say that the model was prevented from over-fitting. Therefore, the model was well trained to classify the
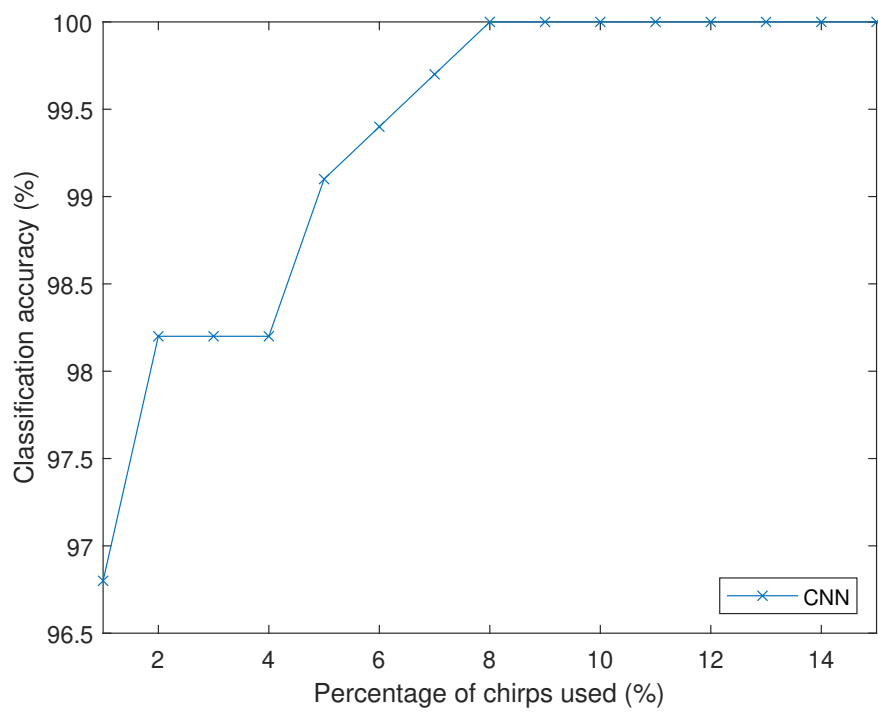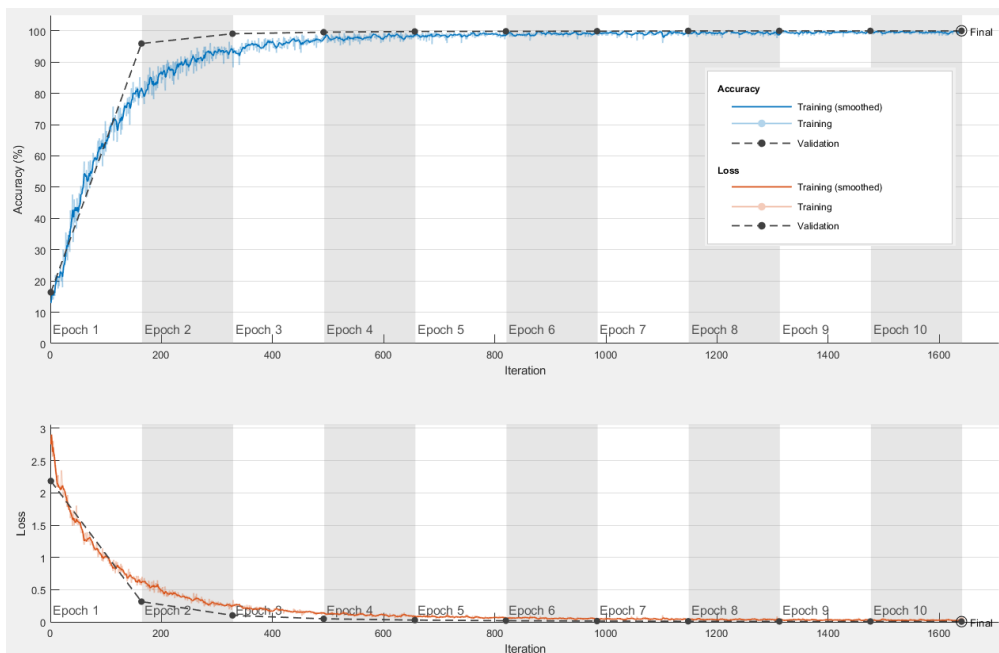
Figure 3.4: Classification accuracy

Figure 3.5: Training and validation accuracy and loss when using 20 chirps

interference signals.

Furthermore, I compared the performance of the model with the methods suggested in [20], [25], which used an SVM for classification. The results are shown in Table 3.11. For comparison, I selected the percentage of chirp used as 8% (20 chirps), which provided a classification performance of 100% for the first time. Compared to two conventional interference classification methods, our proposed method had a better performance. Summarizing the results of Fig. 8 and Table 3.11, our model is more suitable for interference classification than the conventional methods even when the number of chirps used is small.

I also compared the computational complexities of the three methods in quantitative way. Because the three methods used different classification model, it is hard to strictly compare the complexity. I analyzed the relative complexities through the execution times of them. These times are measured with a MATLAB 2019a program on a computer with an AMD Ryzen Threadripper 2990WX 32-Core Processor running at 3.0 GHz. As shown in Table 3.11, our proposed method took longer time to train than the SVM method in [20] using a linear kernel. However, the training was completed in less time than the method of [25] using a quadratic kernel. When comparing the test time, the results of the three methods are similar in tens of milliseconds.

Table 3.11: Performance comparison when 20 chirps used

Method	Accuracy	Training time	Test time
Proposed CNN method	100%	350 s	45.8 ms
SVM method in [8]	75.9%	309 s	20.5 ms
SVM method in [9]	94.4%	2,339 s	11.4 ms

In addition, I verified the performance of the proposed model using 3% of entire chirps (7 chirps), and the result is shown in Fig. 10. As shown in the figure, most of the test samples were well classified, but some data in classes "TS" and "SC" were misclassified. As shown in Fig. 5, the data in class "SC" do not have dominant patterns

of vertical stripes unlike other interference signals. I observed that when the number of chirps used is small, part of the samples in class "SC" is similar to those of class "TS" with noise. I also found that this tendency gradually disappeared as the number of chirps used for classification increased.

Confusion matrix of CNN model

Output class	TS	UC	SC	FC	PC	FSK
TS	99.2	0	0.73	0	0	0
UC	0	100	0	0	0	0
SC	0.8	0	99.27	0	0	0
FC	0	0	0	100	0	0
PC	0	0	0	0	100	0
FSK	0	0	0	0	0	100

Actual class
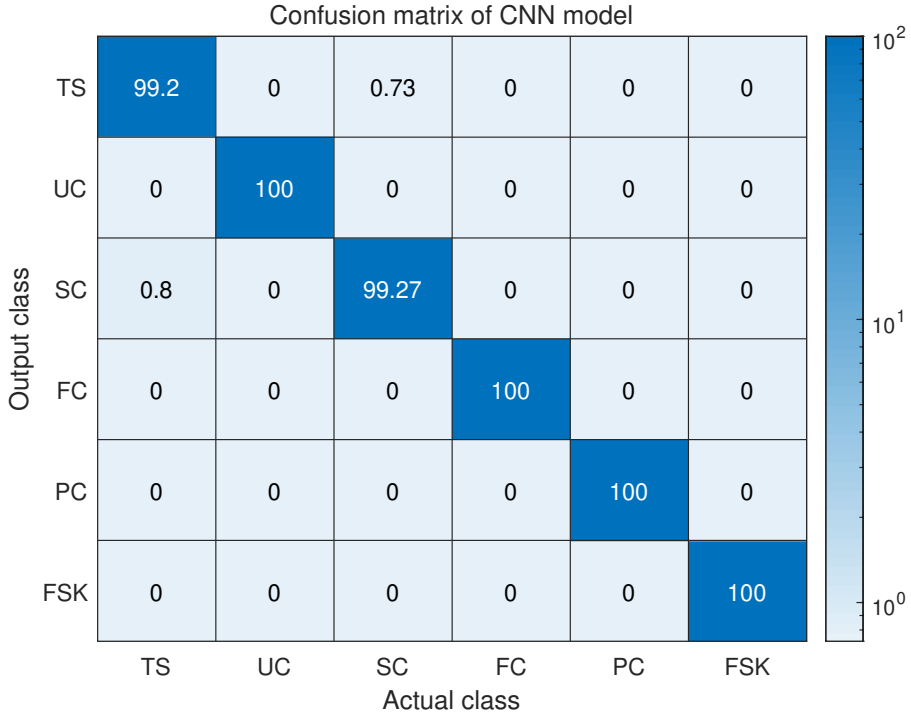
Figure 3.6: Confusion matrix when 7 chirps used

Fig. 11 represents data visualization using t-stochastic neighbor embedding (t-SNE), which uses stochastic probability to achieve dimensionality reduction. The algorithm preserves the characteristics of the original data even after the dimension of data is reduced to two or three [44]. Figs. 11(a) and (b) show the results of the input and the feature vector, respectively. As shown in Fig. 11(a), some data of each class are located close to each other, but many are mixed and distributed. When the features extracted through the CNN model are used as inputs to the t-SNE algorithm, as shown in the Fig. 11(b), the data of each class are distributed in clusters. Therefore, it is evi-

dent that the proposed CNN model appropriately changed the phenotype of the input image for classification.
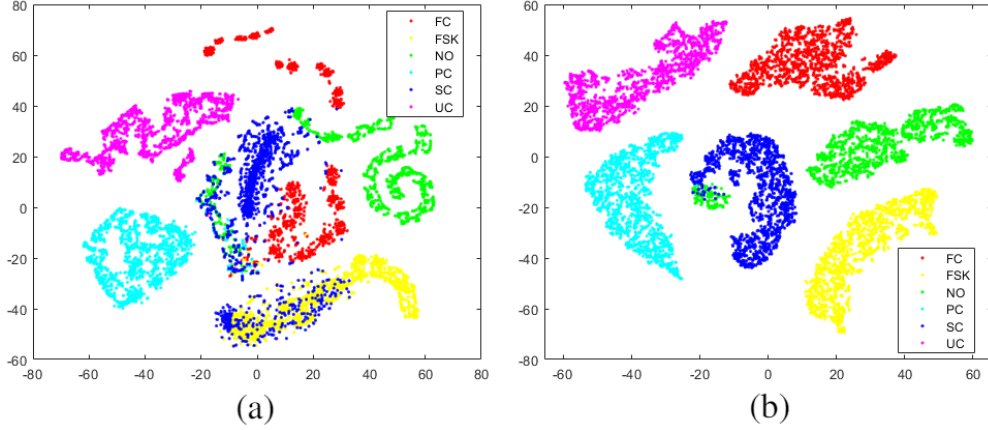
Figure 3.7: Scatter plots of t-SNE algorithm (a) with input data (b) with feature vector

3.4 Summary

In this chapter, I propose methods for identifying the existence of interference signals and classifying their modulation type in the time domain and the frequency domain. For the time-domain method, I first formulated a mathematical signal model in which the target and the interference signals were received together. I extracted five features from time-domain signals using five different modulations. Through an SVM classification, I identified the existence of interference signals and classified the types of modulation. I verified the performance of the proposed method through simulations. The simulation results verified that the identification of the existence of interference signals is possible. Then, I classified the identified received signals into five different types of modulations with an accuracy of over 96%. I also compared the performance of the SVM method with that of the decision tree method. I then verified which feature is the most important for classification among the proposed features.

In the case of frequency-domain method, I used the CNN model to classify five different modulation types of radar interference signals. Using the 2D Fourier transform, the received signals were converted to range-Doppler responses and stored as a set of image data. I proposed the interference signal classifier using the CNN model based on the generated image data set. I verified that the model identified the modulation type of interference signal with an accuracy of over 96%. In addition, the classification performance of the proposed method was also evaluated using a small number of chirps and it showed more than 5.6%p better performance than the conventional SVM's. Through the proposed method, the modulation types of interference signals from various automotive radar sensors are accurately identified in a short time, so it can be effectively applied to the interference mitigation or interference avoidance. I expect increasing diversity in automotive radar systems will lead to a rise in the importance of techniques for identifying and classifying interference signals in the future.

Chapter 4

Interference Mitigation Algorithm in Time-domain Signals

4.1 Introduction

In this section, I will introduce an interference mitigation method. As mentioned in Section 2.2.3, the interference signals increase the noise floor, resulting in degradation of target detection performance. Therefore, interference mitigation is required for target detection, and several mitigation methods have been proposed [45–48]. These mitigation methods can be performed in either the time domain or frequency domain. In the case of time-domain algorithms, the interference signal is mitigated or the target signal is restored with information of nearby target signal. The interval in which an interference signal is received is first detected, and then interference suppression is performed.

In general, the CFAR algorithm is used for target estimation in radar systems [49]. In target estimation, it becomes a problem of distinguishing the target signal from the ambient noise. In a situation where the target signal and the interference signal exist together, it can be changed to the problem of distinguishing the strong interference signal from the target signal, as described in Chapter 2. I used a CNN model to distin-

guish the interference signal from the target signal. I trained the CNN model to extract strong interference signals, and through this step, I can identify the interval where the interference signal was received.

After recognizing the interval, interference mitigation is conducted. Conventional interference mitigation schemes significantly lower the noise level of the frequency response, making it possible to detect a target signal that is obscured by an interference signal. However, these methods create residual signal components while suppressing interference signals. I proposed a method that suppresses the residual component while reducing the noise level caused by the interference. The method is based on phase compensation obtained from velocity estimation.

Also, most time-domain interference mitigation methods reconstruct signals using time samples. In the FMCW radar systems, the interference signal is generated when the frequency of the interference signal overlaps within the linearly increasing transmission frequency band. Therefore, several consecutive time samples are affected by the interference signal. This results a substantial loss of data. However, when changing the signal processing domain from fast time axis to slow time axis, the data loss became non-consecutive and sparse. Based on this concept, I suggested an interference mitigation method.

The remainder of this section is organized as follows. In Section 4.2, a CNN model that estimates the interference interval is introduced. Then, I propose the interference mitigation scheme in Section 4.3. Also, the conventional interference mitigation methods are introduced. In Section 4.4, I compared the results of interference interval estimation and interference mitigation using simulation-based data and measured data. Finally, I conclude this chapter in Section 4.5.

4.2 Detection of Interference Interval in Time-Domain Samples

In this section, I will introduce the forementioned interference signal detection method. For mitigating interference signals in time the domain, it is necessary to find out the interval where the interference signal is received in advance. In particular, because the interference mitigation performance is highly dependent on the interval detection result, this step is important. When conducting target estimation in common automotive radar systems, noise signal and target signal are distinguished in the frequency domain for target estimation. Likewise, one can detect interference signal by distinguishing the interference signal from the target signal in time domain.

4.2.1 Detection with Constant False Alarm Rate

CFAR is one example of a square-law detector. It decides the detection threshold by estimating the noise level using reference cells while keeping constant false alarm rate. The CFAR algorithm needs to adjust the parameters including the size of the reference cells and the size of the guard cells to achieve good performance. The size of the reference cell is determined according to the spacing between adjacent signals. Also, the size of the guard cell is determined considering how many bins the signal to be detected are distributed over. In automotive radar systems, the CFAR algorithm is used in the frequency domain for target estimation. The parameters of the algorithm are set according to the driving environment of the vehicle. In the case of the interference signal, the distribution of the signal may vary greatly according to the system parameters of the interference vehicle, even in the same driving environment.

4.2.2 Detection with Advanced Weighted-Envelope Normalization

An advance weighted-envelope normalization (AWEN) algorithm is proposed in [46]. The algorithm calculates the envelope of the signal using a forward-sliding window

and a backward-sliding window. Then, threshold values for distinguishing between interference signals and target signals are calculated.

4.2.3 Detection with CNN Model

Unlike early machine learning models, deep learning models are characterized by having multiple layers, and lots of models are designed so that the size of the transmitted information vector or matrix become smaller as the layers become deeper. In contrast to this, an autoencoder model consists of a symmetrical structure with inner layers, which make the dimension of the output value equal to that of the input value. Layers from the input layer to the middle layer are called the encoder, and layers from the middle layer to the output layer are called the decoder. The encoder efficiently reduces the dimension so that the input value can be expressed well, and decoder restores the output value from the reduced dimensional information to represent the input value similarly.

Passing through the encoder and decoder in sequence, the autoencoder model can extract meaningful representations of the input. Depending on the learning strategy, the autoencoder model can perform anomaly detection that finds outliers of the data [50], or can be a denoising autoencoder that eliminates noise from the data [51], [52]. The autoencoder models are classified into unsupervised learning. For detecting outliers in time-domain signals, I proposed a bottleneck structured CNN by taking the structure of the autoencoder model, and trained the network with supervised learning.

The structure of the proposed network is shown in Fig. 4.1. I checked the detection performance for various models by changing the hyperparameters of the model, and selected the best model. The performances of various models are shown in Section 4.4.1. The detailed description of each layer is listed in Table 4.1. The dimension of the input data is 32768 x 3 which is the value of the number of chirps multiplied by the number of samples per chirp and 3 channels of data. The real part, the imaginary part, and the power of the signal are used as the 3 channels of data. Examples of
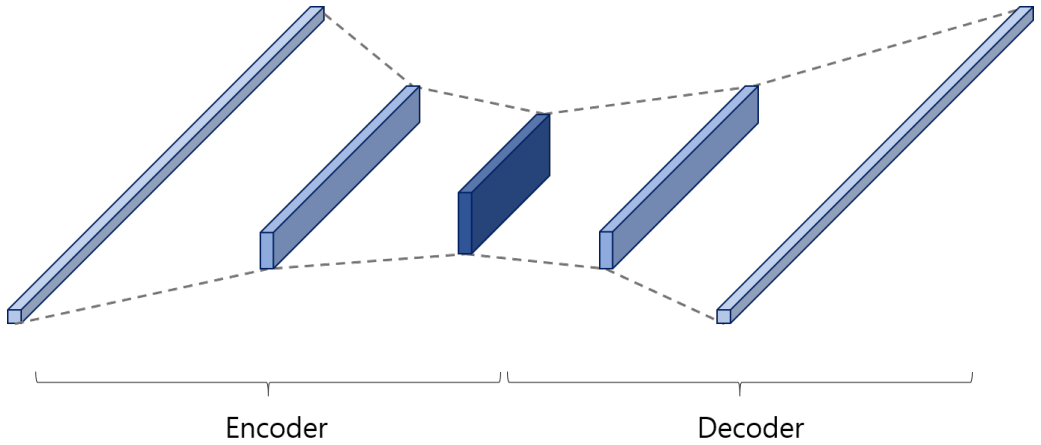
Figure 4.1: Structure of proposed CNN model

input data and output data are shown in Fig.4.2. 3 channels of one signal frame in which the target signal and the interference signal are received together are used as the input. In the case of the output of model, I used a sequence in which the interference interval is replaced by 1. By setting the input and output values in this way, the model is trained to detect the interval where the interference signal was received. Because the interference signals are only observed in a partial portion of the entire sequence, I used the convolutional layers, which are suitable for extracting local characteristics of the signal, rather than using fully connected layers. Binary cross entropy is selected as the loss function of the model, and the ADAM optimizer is used for gradient descent method.

4.3 Interference Signal Mitigation with Velocity Estimation-based Phase Correction

In this section, I will introduce interference mitigation techniques that suppress the detected interference signal or restore them using target signals.

Table 4.1: The detailed description of CNN model

Layer	Size of Feature Map	Size of Filters
Input data	32768 x 3	
1D Conv	32768 x 32	16 x 32
ReLU activation	32768 x 32	
Maxpooling	16384 x 32	2
1D Conv	16384 x 64	16 x 64
ReLU activation	16384 x 64	
Maxpooling	8162 x 64	2
1D Transposed Conv	16384 x 64	16 x 64, stride 2
ReLU activation	16384 x 64	
1D Transposed Conv	32768 x 32	16 x 32, stride 2
ReLU activation	32768 x 32	
1D Conv	32768 x 1	16 x 1
Sigmoid activation	32768 x 1	
Output	32768 x 1	

4.3.1 Conventional Interference Mitigation Methods

Zeroing

This method is the simplest method, replacing the detected interference signal with zeros. Also, it often become a baseline for other restoration methods [45].

Ramp filtering

Ramp filtering was first introduced in [47]. This method performs interference mitigation in the frequency domain by manipulating the magnitude of the frequency response. A nonlinear operator is applied to each range bin over every chirp. The nonlinear operator could be the lower envelope or some sliding window statistics, and many
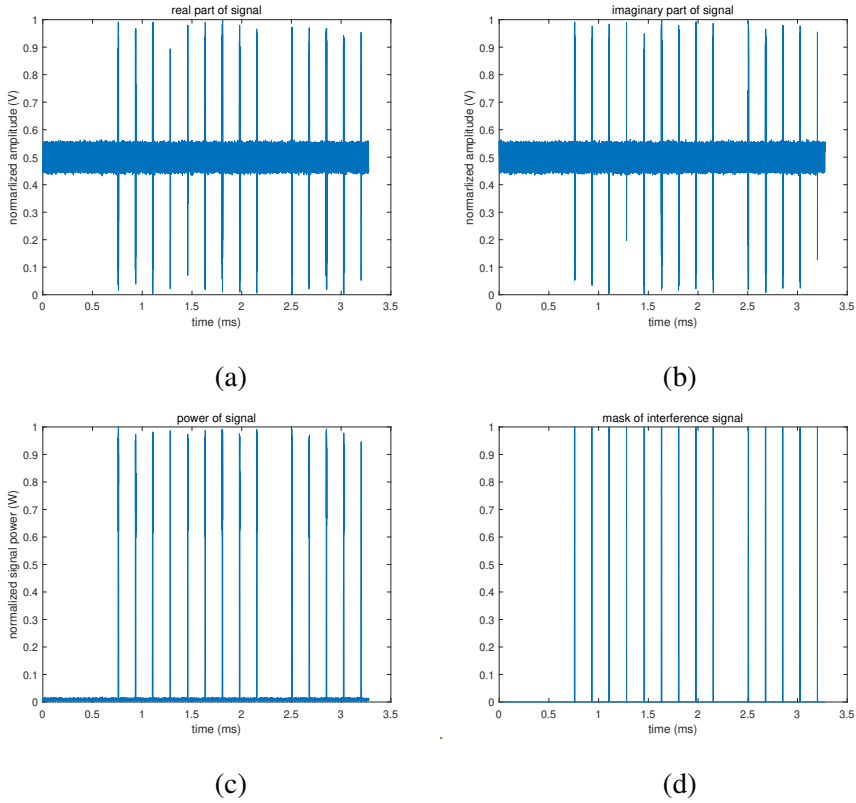
(a)   (b)

(c)   (d)

Figure 4.2: Input and output signals used for training CNN model

studies chose the minimum operator for interference mitigation [45, 47].

Iterative method with adaptive thresholding

Interference mitigation method using iterative method with adaptive thresholding (IMAT) algorithm was introduced in [48]. The basic idea comes from iteratively reconstructing sparse signals with domain transformation.

These conventional methods produce residual frequency components around the target signal when lowering the entire frequency responses of the interference signal. This phenomenon is shown in Fig. 4.3. As shown in the figure, both methods lower the level of the noise floor, but introduce artifacts along the velocity axis. These remainders

could be mistaken as targets in the target detection step and cause false alarms. A more detailed analysis will be dealt with in the Section 4.4.1.
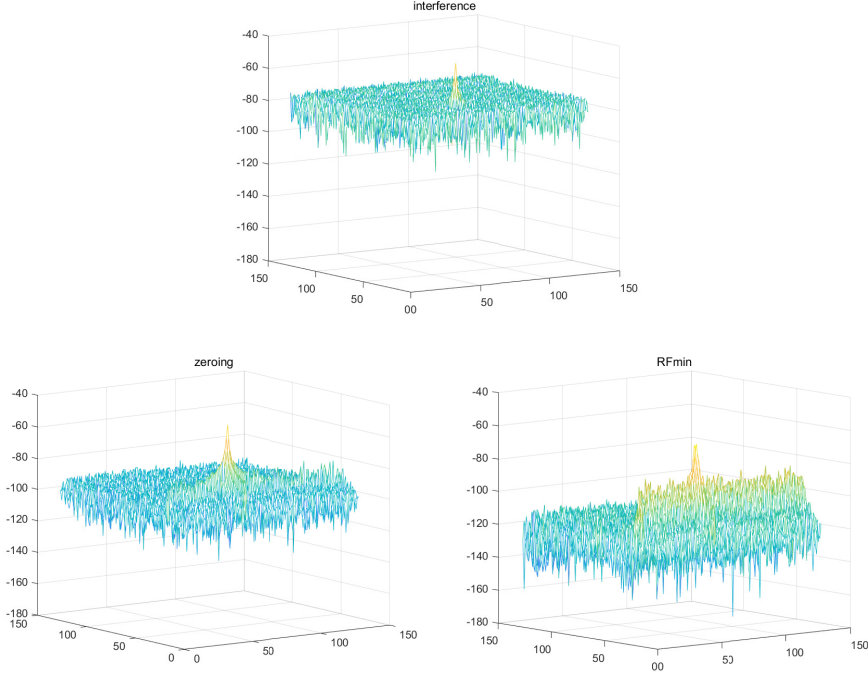

Figure 4.3: Frequency responses of interference signal and mitigated signals

4.3.2 Proposed Velocity Estimation-based Signal Reconstruction

In this section, I will propose a method that reduces the residual frequency components while lowering the noise floor caused by interference signals. The algorithm proceeds in two steps. First, to reconstruct signals in the interference interval, phase compensation based on velocity estimation is conducted. This is a rough approximation of the target signal. Then, more precise reconstruction based on dominant Doppler frequencies is conducted.

Most conventional time-domain signal reconstruction methods have been applied to sampled data in the time axis. In other words, methods including IMAT treats data

according to the fast time axis. Fig. 4.4 shows the positions of samples where the interference signal is received in one frame data matrix. When I try to restore the data of the chirp index near number 120, I have to create more than 80% of the data with the remaining data. This makes it difficult to expect proper generation of data. Therefore, rather than using the data from each column of the matrix, I suggest using data from each row of the matrix. The data sequence to be processed becomes data sequence sampled with chirp time ΔT. By changing the axis of signal processing, I can increase the number of known data that can be used for data reconstruction and reduce the number of unknown data to be generated.
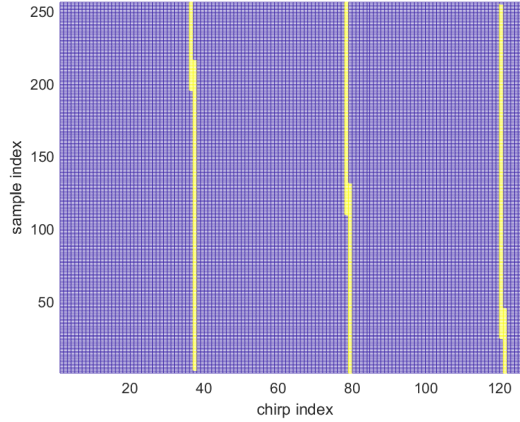

Figure 4.4: Interference intervals masked with 1

The algorithm assumes that the interference signal has been correctly identified in the previous step. Then, the detected interference signals are replaced with zeros. With, indicator matrix $\mathbf{I}$, the resulting signal matrix $\mathbf{Z}$ can be expressed as

$$\mathbf{Z} = \mathbf{S} \bullet \mathbf{I}, \tag{4.1}$$

where $\mathbf{S}$ is received signal matrix in Eq. (2.6), $\bullet$ is Hadamard product which computes element-wise multiplication, and $\mathbf{I}$ is $N \times M$ matrix where $i(n, m)$ is 0 if $s(n, m)$ has interference signal, otherwise 1. Then, the remaining signal $\mathbf{Z}$ becomes interference-

free target signal. Therefore, the velocities of targets can be estimated by taking row-wise Fourier transforms. The corresponding frequency responses can be expressed in a $N \times M_r$ matrix form, where M_r is the number of points in the row-wise Fourier transform, as

$$
\mathbf{X}_r = \begin{bmatrix} \boldsymbol{x}_r(1) \\ \boldsymbol{x}_r(2) \\ \vdots \\ \boldsymbol{x}_r(N) \end{bmatrix}, \tag{4.2}
$$

where $\boldsymbol{x}_r(n) = [x_r(n,1), \cdots, x_r(n,N_r)]$ is the frequency response of $\boldsymbol{z}_r(n)$, which is n_{th} row vector of $\mathbf{Z}$ and $x_r(n, n_r)$ is defined as

$$
x_r(n, n_r) = \sum_{m=1}^{M} z(n,m) \exp\left(-j\frac{2\pi m}{N_r} n_r\right). \tag{4.3}
$$

The resulting frequency response $\boldsymbol{x}_r$ implies the Doppler frequency of targets. However, as shown in Fig. 4.3, signals containing several zeros have unwanted frequency components according to velocity axis. For releasing these phenomenon, I suggested that the phase compensation method using velocity estimation to fill the zero signals. The signals of chirp which has zero signals can be expressed as

$$
\boldsymbol{z}_c(m_{zero}) = \boldsymbol{s}_c(m_{zero}) \cdot \boldsymbol{i}_c(m_{zero}), \tag{4.4}
$$

where $\boldsymbol{z}_c(m)$, $\boldsymbol{s}_c(m)$, $\boldsymbol{i}_c(m)$ are m_{th} column vectors of $\mathbf{Z}$, $\mathbf{S}$, $\mathbf{I}$, respectively, and m_{zero} is the index of the chirp, which contains zeros because the interference signals received. Then, find the nearest chirp index m_{one}, of which $\boldsymbol{i}_c(m_{one})$ is all one vector. As shown in (2.5), the phase difference between two adjacent chirps is $\frac{2f_c v \Delta T}{c}$. Therefore, If I took a maximum value of frequency response $\boldsymbol{x}_r$, I can estimate the velocity $\hat{v}$. Then, the phase difference $\Delta\phi$ between two chirps, m_{zero} and m_{one}, can be expressed as

$$
\Delta\phi = \frac{2f_c \hat{v} \Delta T}{c}(m_{zero} - m_{one}). \tag{4.5}
$$

Therefore, using (4.4) and (4.5), a reconstructed signal $\bar{z}_c(m_{zero})$ for step one can be expressed as

$$\bar{z}_c(m_{zero}) = z_c(m_{zero}) + s_c(m_{one}) \exp\left(j2\pi\Delta\phi\right) \cdot (1_c - i_c(m_{zero})), \qquad (4.6)$$

where $\bar{z}_c(m_{zero})$ is column vector of reconstructed signal matrix $\bar{Z}$, and 1_c is all-ones vector in $\mathbb{R}^{N \times 1}$. Signal process from (4.2) to (4.6) are repeated for each chirp index m which contains interference signals.

If there is only one ideal point-source target which produces a single narrow peak Doppler-domain, the processes up to this point is sufficient for reconstruction. However, in the real world scenario, the frequency response by one target can be spread out. Also, if there are multiple targets, multiple Doppler frequencies will appear, so it is not enough to reconstruct signal with only one maximum value of x_r. Therefore, a second step is required for more accurate signal reconstruction.

As mentioned before, the reconstruction method uses the row vectors of signal matrix. Row-wise Fourier transforms are applied to each row of $\mathbf{barZ}$ as

$$\bar{\mathbf{X}}_r = \begin{bmatrix} \bar{x}_r(1) \\ \bar{x}_r(2) \\ \vdots \\ \bar{x}_r(N) \end{bmatrix}, \qquad (4.7)$$

where $\bar{x}_r(n) = [\bar{x}_r(n,1), \cdots, \bar{x}_r(n, N_r)]$ is the frequency response of $\bar{z}_r(n)$, which is n_{th} row vector of $\bar{Z}$ and $\bar{x}_r(n, n_r)$ is defined as

$$\bar{x}_r(n, n_r) = \sum_{m=1}^{M} \bar{z}(n,m) \exp\left(-j\frac{2\pi m}{N_r} n_r\right). \qquad (4.8)$$

Then, velocity estimation can be performed with operator $f(\cdot)$ and it can be expressed as

$$\boldsymbol{d} = f\left(\bar{\boldsymbol{x}}_r(n)\right) \qquad (4.9)$$

$$= [d(1), d(2), \cdots, d(N_r)],$$

where $\boldsymbol{d}$ is a vector representing detected results, and $d(n_r)$ is 1 if frequency response $\bar{x}_r(n, n_r)$ is detected as target signal, otherwise 0. I chose one-dimensional detector $f(\cdot)$ as the CFAR detector in this study. With Hadamard product, the detected frequency signals $\bar{\boldsymbol{x}}_d$ can be expressed as

$$\bar{\boldsymbol{x}}_d = \bar{\boldsymbol{x}}_r \bullet \boldsymbol{d}. \tag{4.10}$$

(Nonzero components of frequency response $\boldsymbol{x}_d$ represent the Doppler shifts caused by the movements of targets.???) Then, an inverse Fourier transform is applied to $\bar{x}_d(n)$ to fill the empty bins of $\boldsymbol{z}_r(n)$. The corresponding time-domain inverse Fourier transformed signal $\boldsymbol{z}_d(n)$ can be expressed as

$$z_d(n, m) = \frac{1}{N_r} \sum_{n_r=1}^{N_r} \bar{x}_d(n_r) \exp\left(j\frac{2\pi n_r}{N_r}m\right). \tag{4.11}$$

Finally, the reconstructed signal $\boldsymbol{z}_{mit}(n)$ can be expressed as

$$\boldsymbol{z}_{mit}(n) = \boldsymbol{z}_r(n) + \boldsymbol{z}_d(n) \bullet (\boldsymbol{1}_r - \boldsymbol{i}_r(n)), \tag{4.12}$$

where $\boldsymbol{1}_r$ is all-ones vector in $\mathbb{R}^{1 \times M}$, and $\boldsymbol{i}_r(n)$ is n_{th} row vector of indicator matrix $\mathbf{I}$ in Eq. (4.1). Signal processes from (4.7) to (4.12) are repeated for all rows of $\mathbf{X}_r$.

4.4   Results

For validating the performance of the interference interval detection and mitigation, a simulation-based verification and the real data-based verification are conducted.

Two evaluation metrics are used for validating the performance of algorithm. First, a signal-to-interference-plus-noise ratio (SINR) represents a relative power of signal to noise floor, which is related to detectability of target signals. SINR can be expressed as

$$\text{SINR} = \frac{\frac{1}{N_O} \sum_{(n,m)\in\mathbb{O}} |\mathbf{X}_{rv}(n, m)|^2}{\frac{1}{N_N} \sum_{(n,m)\in\mathbb{N}} |\mathbf{X}_{rv}(n, m)|^2}, \tag{4.13}$$

where $\mathbb{O}$ is a set of objects, $\mathbb{N}$ is a set of noise signals including interference signals, N_O is the number of objects in the set $\mathbb{O}$, N_O is the number of elements in the set $\mathbb{N}$, and $\mathbf{X}_{rv}$ is the range Doppler response. The SINR is related to a detection probability because it indicates how strong the target's response is relative to ambient noise and interference signals.

Also, an error vector magnitude (EVM) was employed to measure how well the values of the target peaks were reconstructed. The EVM can be expressed as

$$\text{EVM} = \frac{1}{N_O} \sum_{(n,m)\in\mathbb{O}} \frac{|\tilde{\mathbf{X}}_{rv}(n,m)| - |\mathbf{X}_{rv}(n,m)|}{|\tilde{\mathbf{X}}_{rv}(n,m)|}. \tag{4.14}$$

The magnitude and phase of the target signal are necessary to estimate the distance, velocity, and angle of the target, and through EVM, it is possible to determine whether the complex values are well preserved.

4.4.1 Simulated Data

In this subsection, I verified the performance of the proposed method by simulated data. The parameters of one ego-vehicle and two interference vehicles set in the simulation is shown in Table 4.2. By overlapping the operating frequency bands of three radars, the interference signals remain after passing the mixer and the low pass filter. Also, to generate more interference signals, I set the chirp slopes of both radars to similar values.

Detection of Interference Interval

First, the detection performance was verified for various models by changing the hyperparameters as shown in Table. 4.3. I compared detection probabilities of models while keeping false alarm rates as 0.0005. When the model consisted of one layer or three layers, the performance dropped significantly below 90%. Among the various models, the 3rd model was selected as the optimal model.

Table 4.2: Parameters of ego-vehicle and interference vehicle

Vehicle	Parameter	Value
Ego-vehicle	Carrier frequency	77 GHz
	Bandwidth	384 MHz
	Sampling frequency	10 MHz
	Number of samples	256
	Sweep time	25.6 μs
	Number of chirps	128
Interference vehicle 1	Carrier frequency	77 GHz
	Bandwidth	400 MHz
	Sweep time	30 μs
Interference vehicle 2	Carrier frequency	77 GHz
	Bandwidth	380 MHz
	Sweep time	25 μs

Table 4.3: Detection probability and false alarm rate of various CNN models

	Number of layers	Size of first filter	Size of second filter	Maxpooling size	Detection probability
1	2	4 x 32	4 x 64	2	0.9530
2	2	8 x 32	8 x 64	2	0.9580
3	**2**	**16 x 32**	**16 x 64**	**2**	**0.9644**
4	2	32 x 32	32 x 64	2	0.9132
5	2	4 x 16	4 x 32	2	0.9540
6	2	16 x 32	16 x 64	4	0.9591
7	2	32 x 32	32 x 64	4	0.9449
8	2	16 x 32	16 x 64	8	0.9475
9	2	32 x 32	32 x 64	8	0.9641

Then, the performance of detection of interference interval is analyzed. The result of the detection is shown in Fig. 4.5(a). The CFAR detector and AWEN method calculated appropriate thresholds for detecting interference signals. Also, the proposed CNN-based detector detected interference signals well.
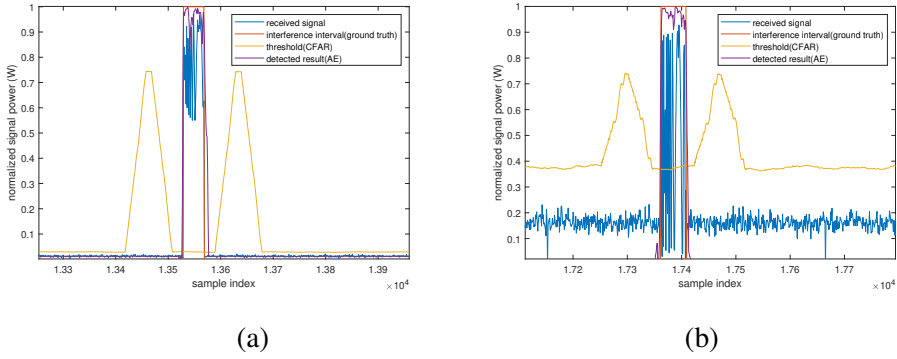

Figure 4.5: Interference interval results

Fig. 4.5(a) is the case when the signal powers of the interference signals and target signals have large difference. As shown in Fig. 4.5(b) when the difference in power between the interference signals and the target signals is reduced, it can be observed that the performances of the CFAR detector and AWEN methods are degraded. This is because even if the interference signal is generated, not all samples of the interference signal have high instantaneous power. The CFAR detector and the AWEN algorithm are vulnerable to this situation because they use the power and envelope respectively to calculate the threshold. However, even in this case, the proposed CNN-based detector detects the interference interval with good performance.

Next, the weakness of CFAR detector is analyzed. As mentioned in Sec. 4.2.1, CFAR detector needs to set the values of the sizes of reference cell and guard cell to achieve good performance. The length of the interference interval is determined by the slopes of two radars. However, the slope of the interference radar can vary by the manufacturers, it is hard to determine the size of guard cell as a specific value. Fig. 4.6 shows the detection result CFAR detector of which the guard cell size is 120. As shown

in the Fig. 4.6(a), for a signal having an interference signal length of 60, the interference interval was accurately estimated by the CFAR detector. However, for the case of Fig. 4.6(b), the interference interval was not detected because the signal had long interference interval compared to the size of the guard cell. It could be worse when multiple interference signals income, making the interference interval even larger. Therefore, I conclude that the CFAR detector is not appropriate for detecting the interference interval in the time domain.
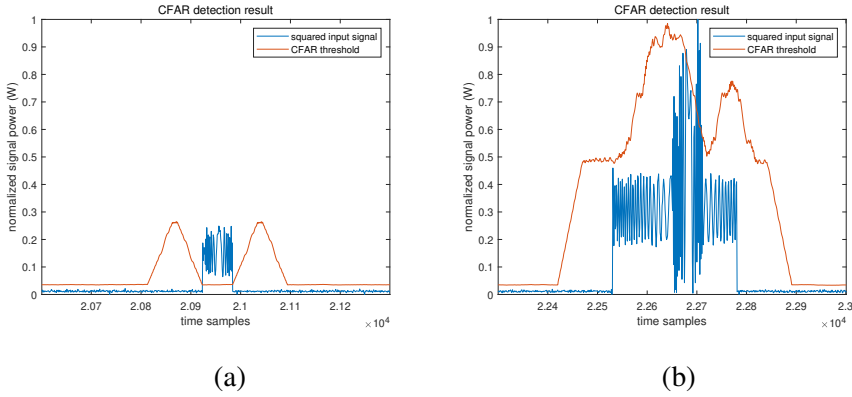

Figure 4.6: Detection results with CFAR detector

The AWEN method and the proposed CNN-based detector relieve this problem. As shown in the Fig. 4.7, which is the same signal of 4.6(b), the AWEN method and the proposed method performed better than the CFAR detector. The results imply that two methods had little influence of parameters of radars.

Finally, the ECDF of the detection probability and false alarm rate is shown in Fig. 4.8. As shown in Fig. 4.8(a), the detection probability of the proposed method showed the best performance. Also, the false alarm rate kept low value as shown in Fig. 4.8(b). Table 4.4 shows average values of the detection probability and false alarm rate of 3 methods. The CFAR detector showed poor performance because there were various length of interference interval and the method depended on the signal power. Compared to the AWEN method, the proposed CNN-based detection method showed

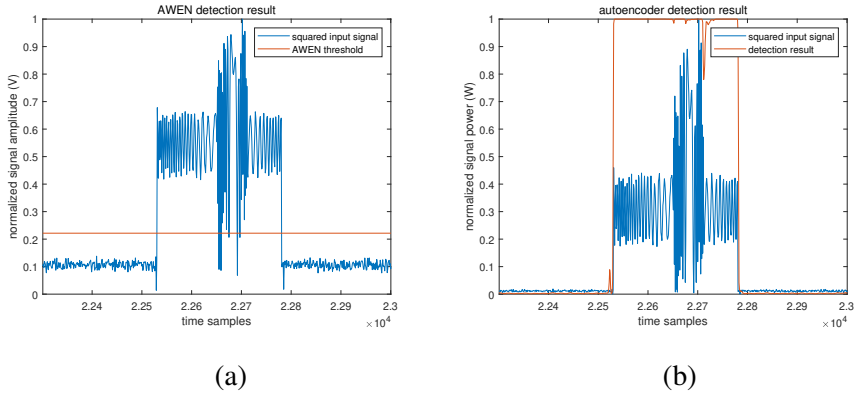better detection probability and lower false alarm rate.

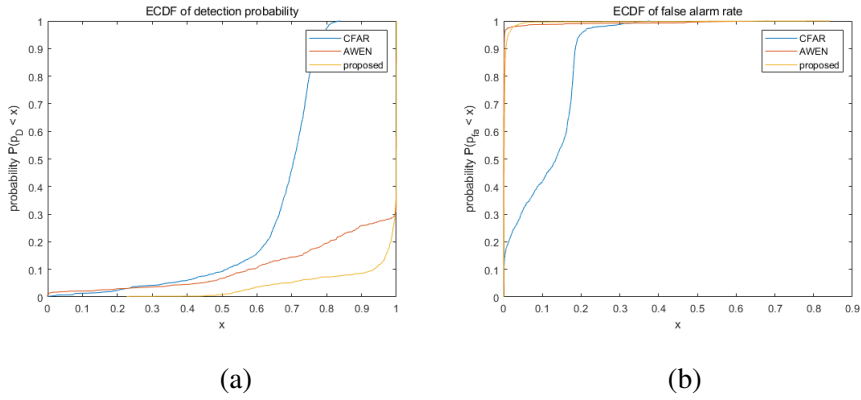Figure 4.7: Detection results with AWEN method and proposed method

Figure 4.8: Empirical cumulative distribution function of (a) detection probability and (b) false alarm rate

Table 4.4: Detection probability and false alarm rate of 3 methods

	CFAR	AWEN	proposed
detection probability	0.6661	0.8950	0.9644
false alarm rate	0.1109	0.0062	0.0050

Signal Reconstruction

Fig. 4.9 shows the range-Doppler responses when one target is at $(R_t, v_t) = (38.4$ m, 20.8 m/s), the first interference radar at $(R_1, v_1) = (20.6$ m, -21.7 m/s), and the second interference radar at $(R_2, v_2) = (5.0$ m, -4.4 m/s). Fig. 4.9(a) is the range-Doppler response when the interference signals were not received. When two interference radars emitted radar signals, the noise floor increased, making target peaks to be obscured as shown in Fig. 4.9(b).

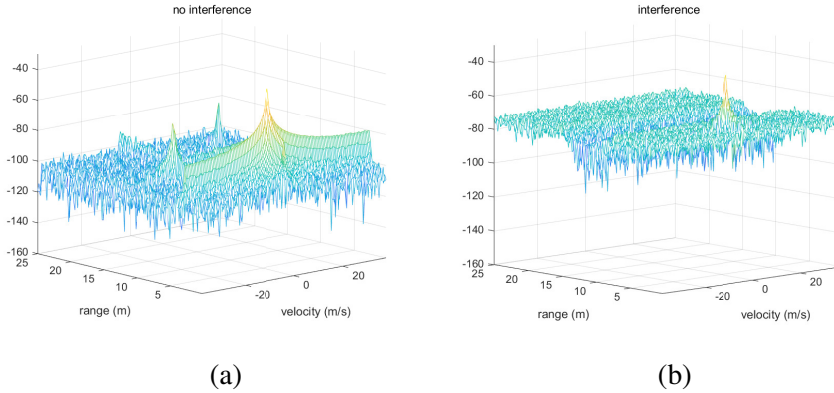(a)   (b)

Figure 4.9: Range-Doppler response of target signal and interference signal

First, a qualitative analysis of interference mitigation performance is introduced. As shown in Fig. 4.10, the target peaks can be observed, which were not detected because of being masked by the response of the interference signals. However, the interference mitigation methods created residual frequency responses. These artifacts were detected by target detectors. As shown in the right column of Fig. 4.10, the CFAR

detector detected the residual frequency responses as targets. For example, the residual frequency responses of RFmin method were sufficient to be detected by the CFAR detector because it had a power 30dB higher than the noise floor. The zeroing method and the IMAT method also generated ghost targets. In the case of the proposed method, it can be seen that the residual components was generated the least. Also, only 3 target peaks were detected by CFAR detector. Furthermore, the frequency response of the proposed method was most similar to the frequency response of the original target signal, especially when comparing the frequency responses generated by target at $(R_2, v_2) = (5.0 \text{ m}, -4.4 \text{ m/s})$. This means the proposed method had reconstructed the target signal properly.

For validating the results in quantitative way, the ECDF of SINR is investigated. As shown in Fig. 4.11, the proposed reconstruction method reached the highest SINR value except the RFmin method. In the case of RFmin method, because it mitigated the interference signals by substituting the magnitudes of every rows of frequency responses with the minimum values of the frequency responses of each row. For this reason, the RFmin method showed high gain in terms of SINR. The statistical results for the SINR are summarized in Table. 4.5. Except RFmin method, the proposed method showed the best performance.

Table 4.5: Interference mitigation performance evaluated by SINR

Mitigation Method	SINR (dB)		
	50%-tile	90%-tile	Mean
Zeroing	40.1266	45.0952	40.6407
RFmin	41.6797	48.0967	42.3060
IMAT	40.3529	45.5957	40.9164
Proposed	40.5442	45.9376	41.1707

Fig. 4.12 shows the ECDF of EVM of each mitigation method. The RFmin method
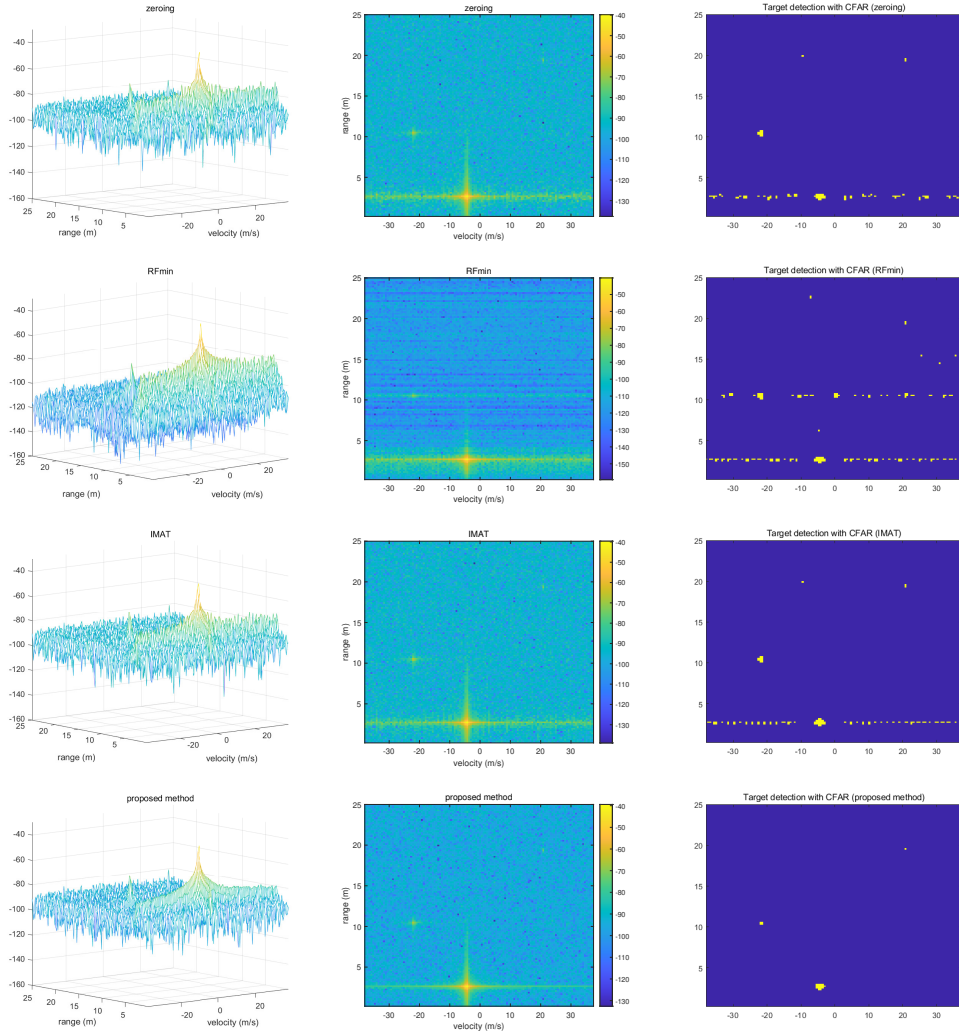
Figure 4.10: Range-Doppler responses after applying 4 interference mitigation methods on simulated data
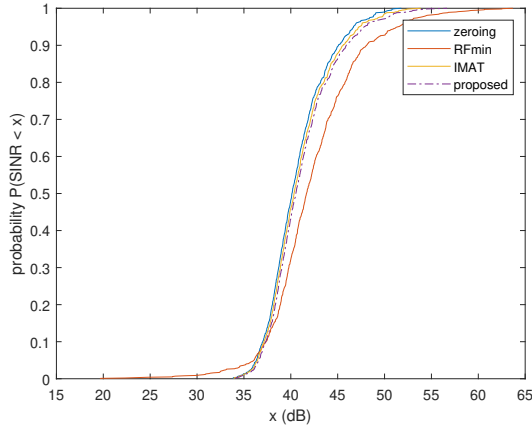
Figure 4.11: Empirical cumulative distribution function of SINR

showed the highest EVM value. This is caused by manipulating the magnitudes of frequency responses. As the intensity of the interference signal was lowered, the intensity of the target signal was also lowered, resulting in a lot of distortion. The statistical results are shown in Table 4.6. When compared to other mitigation methods, the proposed method showed the least EVM error. Low EVM value can lead to a small error in the angle estimation performed after the range-velocity estimation. Table 4.6 shows the statistical values of each mitigation methods. Among the entire methods, the proposed method shows the best performance.

Table 4.6: Interference mitigation performance evaluated by EVM

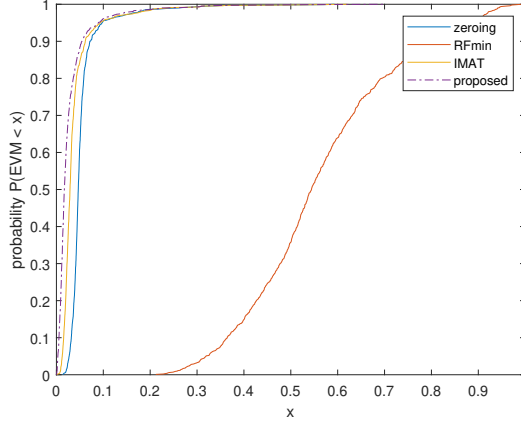| Mitigation Method	EVM		
	50%-tile	90%-tile	Mean
Zeroing	0.0466	0.0721	0.0547
RFmin	0.5441	0.7950	0.5639
IMAT	0.0289	0.0616	0.0392
Proposed	0.0169	0.0545	0.0292

Figure 4.12: Empirical cumulative distribution function of EVM

Angle Estimation

With multiple receiving antennas, the angle of the target can be estimated. Phase differences between adjacent receiving antennas are induced and angle estimators estimate the direction of arrival (DoA) using these phase differences. Therefore, it is important to verify that the phase differences between the antennas are preserved even after interference mitigation. I supposed that the radar system had 8 receiving antennas, and the angle of the targets were varying between $(-30°, 30°)$.

Fig. 4.13 shows an example of angle estimation when one target is at $(R_t, \theta_t) = (10.2 \text{ m}, -24.5°)$, the first interference radar at $(R_1, \theta_1) = (16.4 \text{ m}, 18.5°)$, and the second interference radar at $(R_2, v_2) = (21.7 \text{ m}, -4.0°)$. It can be seen that DoAs were properly estimated.

RMSE values of angle estimation of 4 different mitigation methods are shown in Table. 4.7. Although the RMSE of the RFmin method is slightly bigger than the other methods, all the four algorithms can estimate the DoA well.

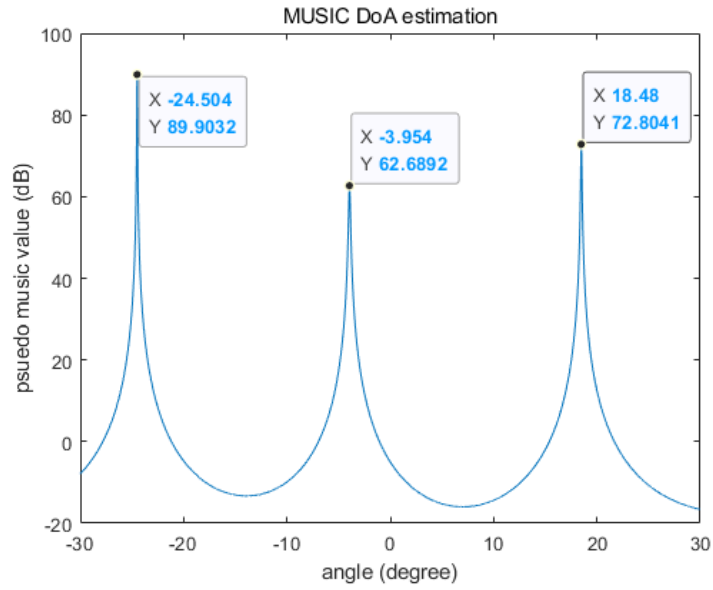Figure 4.13: MUSIC DoA estimation result when 1 target and 2 interference radar are in the FoV of radar

Table 4.7: RMSE of angle estimation

Method	Zeroing	RFmin	IMAT	Proposed
RMSE (°)	0.17	0.23	0.17	0.17

4.4.2 Measured Data

I conducted data measurement for validating the proposed method. Fig. 4.14 shows the measurement environment. Two TI AWR1642 radars were used, one for performing target estimation and the other for generating an interference signal. The victim radar was mounted on a cart and moved back and forth. The interference generating radar was at fixed point. Two pedestrians moved within the field of view of the detection radar. Two radars share the frequency bands to generate the interference signals. Other parameters are listed in Table 4.8.
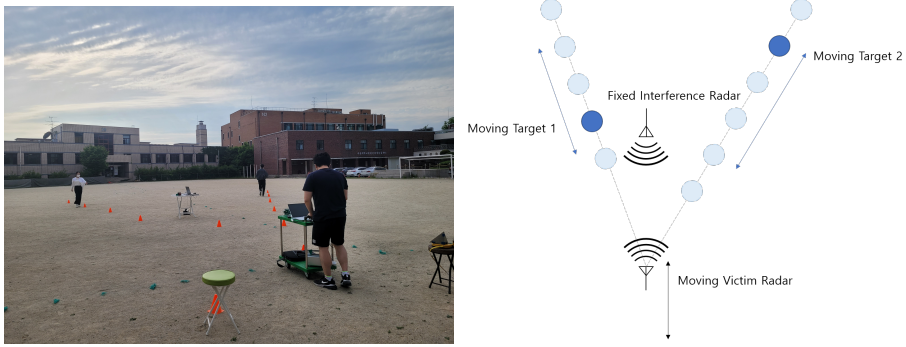

Figure 4.14: Experimental environment

Detection of Interference Interval

First, I investigated the performance of interference interval detection. As shown in the Fig. 4.15, interference signals were received at sample indices that were approximately from 18000 to 19920. Although the signal power near the sample index around 19920 was weak, there was no guarantee that the interference signal was not received, so it is better to detect it as the interference interval. From this point of view, the CFAR detector and the AWEN method made false decision, as the threshold was low. However, in the case of the proposed CNN-based detector, when setting the decision threshold as 0.5, the detector found the interference interval as intended.

Table 4.8: Parameters of radars used in measurement

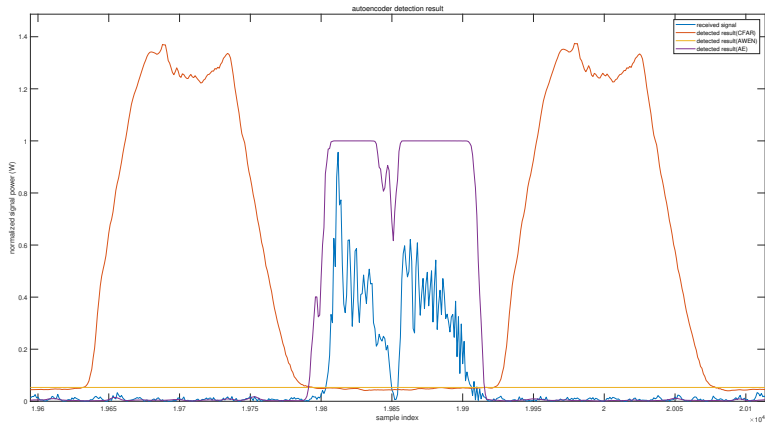| Radar	Parameter	Value
Victim radar	Carrier frequency	77 GHz
	Bandwidth	384.4 MHz
	Sampling frequency	10 MHz
	Number of samples	256
	Sweep time	25.6 us
	Number of chirps	128
Interference radar	Carrier frequency	77 GHz
	Bandwidth	639.2 MHz
	Sweep time	40 us

Figure 4.15: Results of interference interval detection

Signal Reconstruction

After identifying the interference interval, the interference mitigation was performed. As shown in the Fig. 4.16, when the interference signals received, the noise floor increased, resulting the targets cannot be detected. Even straight lines in the frequency response can be detected as targets.
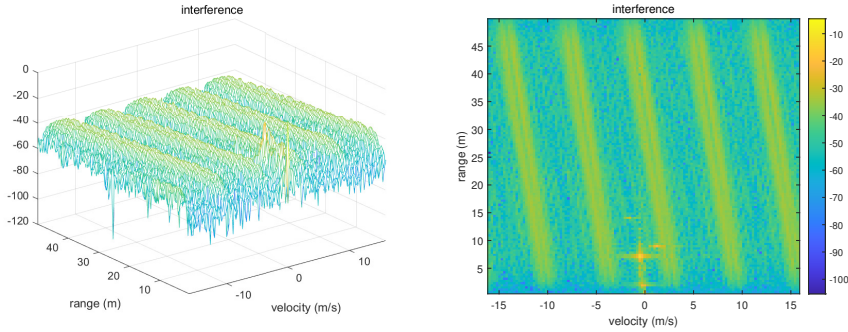

Figure 4.16: Range-Doppler response of interference signal

Fig. 4.17 shows the range-Doppler responses of 4 interference mitigation methods. As shown in the figure, the RFmin method created the residual frequency responses the most. Even, the target near 15 m was disappeared while mitigation. The zeroing method and IMAT method showed similar results. Both methods created peak-like responses, which can be detected as ghost targets. Those peak-like responses were detected by the CFAR detector. In the case of the proposed method, the residual frequency responses were hardly found, while lowering the noise floor caused by the interference signal. Also, the ghost targets which were generated in conventional cases were not detected by CFAR detector.

The ECDF of SINR is shown in Fig. 4.18. Similar to the result of the simulated data, the RFmin method showed the best performance in this aspect. However, the RFmin method created the artifacts the most, resulting high false alarm rate. Among the remaining methods, the proposed method showed the best performance. The statistical results are shown in Table 4.9. The proposed method improved the SINR in 8 dB

compared to the interference signal. Also, the proposed method increased the SINR more than $0.5\,\mathrm{dB}$ compared to the IMAT method.

Table 4.9: Interference mitigation results evaluated by SINR

Mitigation Method	SINR (dB)		
	50%-tile	90%-tile	Mean
Interference signal	28.5497	37.1026	29.8233
Zeroing	36.5526	38.2744	36.6435
RFmin	49.3905	52.4543	49.3303
IMAT	37.0172	38.5211	37.0189
Proposed	37.8624	39.0938	37.8315

Angle Estimation

Finally, plausibility of angle estimation in measurement data is verified. As shown in the Fig. 4.14, 2 targets and 1 interference radar is in the field of view (FoV) of the victim radar. An angle of the first target θ_1 was set to be smaller than an angle of the second target θ_2. Fig. 4.19 shows the MUSIC estimation results of three objects. As shown in the figure, the estimated angle of the interference radar $\hat{\theta}_I$ is 0.71°, which is close to 0°. Also, $\hat{\theta}_2$ has larger value than $\hat{\theta}_1$. In conclusion, it was verified that target estimation is possible after interference mitigation in the measured data.

4.5 Summary

In this chapter, I proposed the interference interval detection method and interference mitigation method. First, I concluded that the CFAR detector is not appropriate for interference interval detection as the intervals vary a lot. I proposed a CNN model to detect anomalies in signals. The model can detect intervals which have strong interference signals. Compared to AWEN method, the proposed method showed 5% higher

detection probability, while keeping lower false alarm rate. Then, I suggested an interference mitigation method which is done at slow time axis. This makes the loss of data become decrease, resulting an improvement in signal reconstruction performance. Furthermore, because some zero signals make the frequency response have distortion, I approximated the missing data by phase compensation. As a result, in both the simulated data and the measurement data, the proposed method lowered the noise floor caused by the interference signal, while suppressing the residual frequency signals to be created. Especially, the proposed method has more than 0.5 dB gain of SINR over the conventional IMAT method.
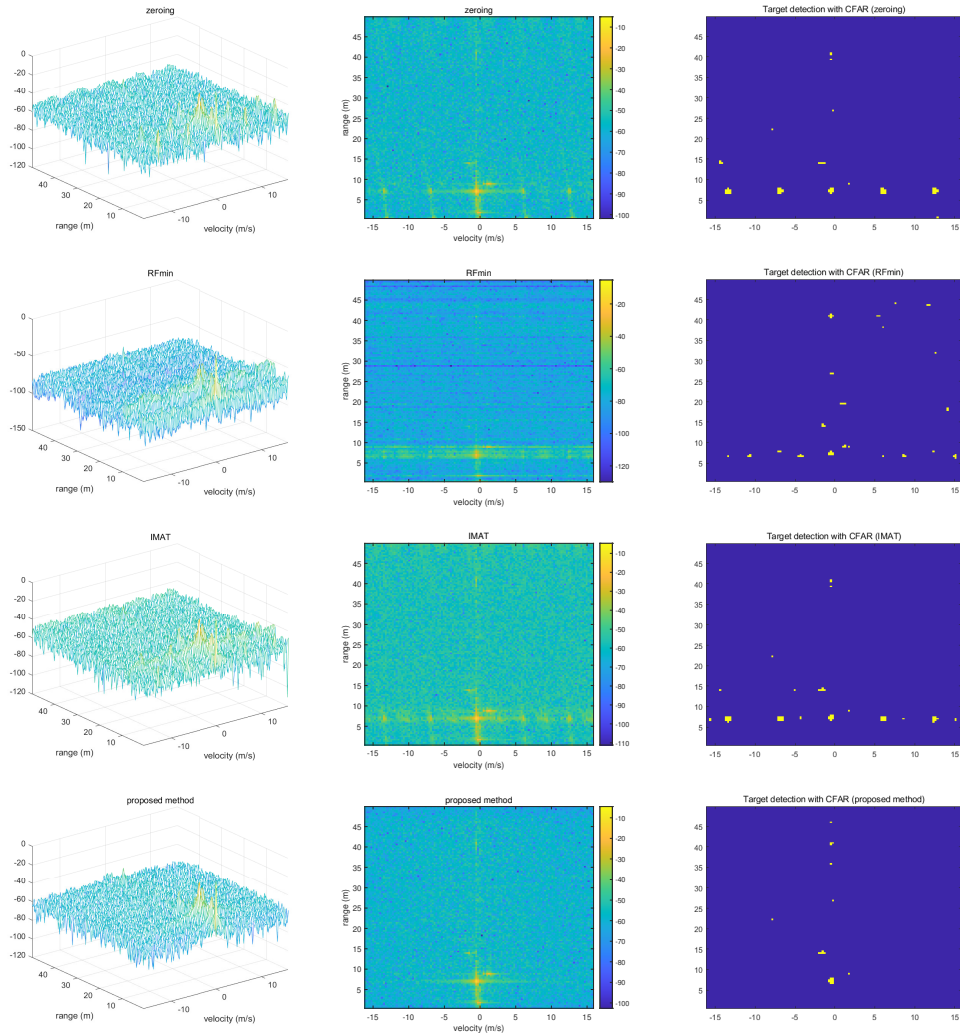
Figure 4.17: Range-Doppler response after applying 4 interference mitigation methods
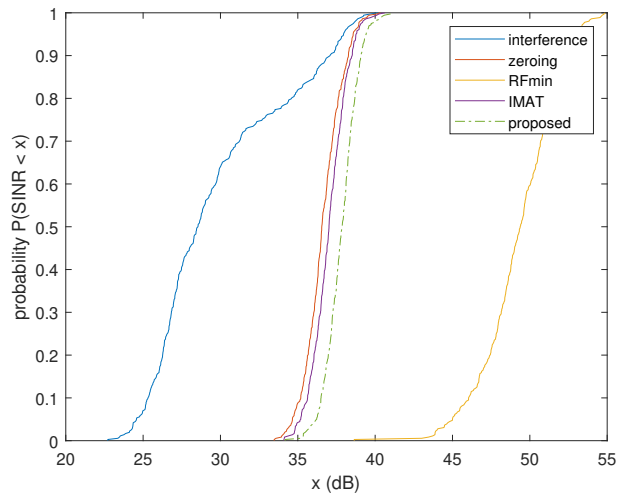
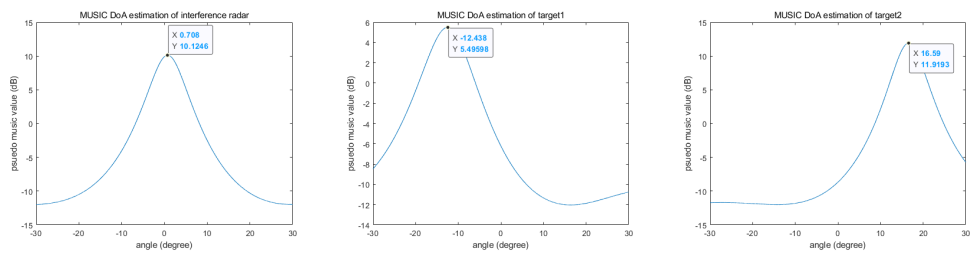Figure 4.18: Empirical cumulative distribution function of SINR

Figure 4.19: DoA estimation results of three objects

Chapter 5

Conclusion

In this dissertation, I proposed a sequence of the interference handling methods. First, I proposed methods for identifying the existence of interference signals and classifying their modulation type in the time domain and the frequency domain. For the time-domain method, I first formulated a mathematical signal model in which the target and the interference signals were received together. I extracted five features from time-domain signals using five different modulations. Through an SVM classification, I identified the existence of interference signals and classified the types of modulation. I verified the performance of the proposed method through simulations. The simulation results verified that the identification of the existence of interference signals is possible. Then, I classified the identified received signals into five different types of modulations with an accuracy of over 96%. I also compared the performance of the SVM method with that of the decision tree method. I then verified which feature is the most important for classification among the proposed features. In the case of frequency-domain method, I used the CNN model to classify five different modulation types of radar interference signals. Using the 2D Fourier transform, the received signals were converted to range-Doppler responses and stored as a set of image data. I proposed the interference signal classifier using the CNN model based on the generated image data set. I verified that the model identified the modulation type of interference signal with

an accuracy of over 96%. In addition, the classification performance of the proposed method was also evaluated using a small number of chirps and it showed more than 5.6%p better performance than the conventional SVM's.

Then, I proposed the interference interval detection method. First, I concluded that the CFAR detector is not appropriate for interference interval detection as the intervals vary a lot. I proposed a CNN model to detect anomalies in signals. The model can detect intervals which have strong interference signals. Compared to AWEN method, the proposed method showed 5% higher detection probability, while keeping lower false alarm rate.

Finally, I proposed an interference mitigation method which is done at slow time axis. This makes the loss of data become decrease, resulting an improvement in signal reconstruction performance. Furthermore, because some zero signals make the frequency response have distortion, I approximated the missing data by phase compensation. As a result, in both the simulated data and the measurement data, the proposed method lowered the noise floor caused by the interference signal, while suppressing the residual frequency signals to be created. Especially, the proposed method has more than 0.5 dB gain of SINR over the conventional IMAT method.

Bibliography

[1] S. M. Patole, M. Torlak, D. Wang, and M. Ali, "Automotive radars: A review of signal processing techniques," *IEEE Signal Processing Magazine*, vol. 34, no. 2, pp. 22–35, 2017.

[2] W. D. Jones, "Keeping cars from crashing," *IEEE spectrum*, vol. 38, no. 9, pp. 40–45, 2001.

[3] J. Dickmann, J. Klappstein, M. Hahn, N. Appenrodt, H.-L. Bloecher, K. Werber, and A. Sailer, "Automotive radar the key technology for autonomous driving: From detection and ranging to environmental understanding," in *2016 IEEE Radar Conference (RadarConf)*.   IEEE, 2016, pp. 1–6.

[4] J. Wenger, "Automotive radar-status and perspectives," in *IEEE Compound Semiconductor Integrated Circuit Symposium, 2005. CSIC'05*.   Ieee, 2005, pp. 4–pp.

[5] M. Schneider, "Automotive radar-status and trends," in *German microwave conference*, 2005, pp. 144–147.

[6] S. Lutz, D. Ellenrieder, T. Walter, and R. Weigel, "On fast chirp modulations and compressed sensing for automotive radar applications," in *2014 15th International Radar Symposium (IRS)*.   IEEE, 2014, pp. 1–6.

[7] S. Heuel, "Automotive radar interference test," in *2017 18th International Radar Symposium (IRS)*.   IEEE, 2017, pp. 1–7.

[8] G. M. Brooker, "Mutual interference of millimeter-wave radar systems," *IEEE Transactions on Electromagnetic Compatibility*, vol. 49, no. 1, pp. 170–181, 2007.

[9] A. Bourdoux, K. Parashar, and M. Bauduin, "Phenomenology of mutual interference of fmcw and pmcw automotive radars," in *2017 IEEE Radar Conference (RadarConf)*.   IEEE, 2017, pp. 1709–1714.

[10] M. Goppelt, H.-L. Blöcher, and W. Menzel, "Automotive radar–investigation of mutual interference mechanisms," *Advances in Radio Science*, vol. 8, no. B. 3, pp. 55–60, 2010.

[11] J. Bechter, M. Rameez, and C. Waldschmidt, "Analytical and experimental investigations on mitigation of interference in a dbf mimo radar," *IEEE Transactions on Microwave Theory and Techniques*, vol. 65, no. 5, pp. 1727–1734, 2017.

[12] Z. Xu and Q. Shi, "Interference mitigation for automotive radar using orthogonal noise waveforms," *IEEE Geoscience and Remote Sensing Letters*, vol. 15, no. 1, pp. 137–141, 2017.

[13] J.-H. Choi, H.-B. Lee, J.-W. Choi, and S.-C. Kim, "Mutual interference suppression using clipping and weighted-envelope normalization for automotive fmcw radar systems," *IEICE Transactions on Communications*, vol. 99, no. 1, pp. 280–287, 2016.

[14] J. Bechter, C. Sippel, and C. Waldschmidt, "Bats-inspired frequency hopping for mitigation of interference between automotive radars," in *2016 IEEE MTT-S International Conference on Microwaves for Intelligent Mobility (ICMIM)*.   IEEE, 2016, pp. 1–4.

[15] S. Lim, S. Lee, J.-H. Choi, J. Yoon, and S.-C. Kim, "Mutual interference suppression and signal restoration in automotive fmcw radar systems," *IEICE Transactions on Communications*, 2018.

[16] J. Jung, S. Lim, J. Kim, S.-C. Kim, and S. Lee, "Interference suppression and signal restoration using kalman filter in automotive radar systems," in *2020 IEEE International Radar Conference (RADAR)*. IEEE, 2020, pp. 726–731.

[17] F. Uysal and S. Sanka, "Mitigation of automotive radar interference," in *2018 IEEE Radar Conference (RadarConf18)*. IEEE, 2018, pp. 0405–0410.

[18] V. Winkler, "Range doppler detection for automotive fmcw radars," in *2007 European Radar Conference*. IEEE, 2007, pp. 166–169.

[19] K.-J. You, H.-E. Jeon, and H.-C. Shin, "Radar modulation identification using inequality measurement in frequency domain," *IEICE TRANSACTIONS on Fundamentals of Electronics, Communications and Computer Sciences*, vol. 100, no. 4, pp. 975–981, 2017.

[20] R. Zhang and S. Cao, "Support vector machines for classification of automotive radar interference," in *2018 IEEE Radar Conference (RadarConf18)*. IEEE, 2018, pp. 0366–0371.

[21] E. Al Hadhrami, M. Al Mufti, B. Taha, and N. Werghi, "Ground moving radar targets classification based on spectrogram images using convolutional neural networks," in *2018 19th International Radar Symposium (IRS)*. IEEE, 2018, pp. 1–9.

[22] A. Palffy, J. Dong, J. F. Kooij, and D. M. Gavrila, "Cnn based road user detection using the 3d radar cube," *IEEE Robotics and Automation Letters*, vol. 5, no. 2, pp. 1263–1270, 2020.

[23] N. Ødegaard, A. O. Knapskog, C. Cochin, and J.-C. Louvigne, "Classification of ships using real and simulated data in a convolutional neural network," in *2016 IEEE Radar Conference (RadarConf)*. IEEE, 2016, pp. 1–6.

[24] X. Zhou, L.-C. Qian, P.-J. You, Z.-G. Ding, and Y.-Q. Han, "Fall detection using convolutional neural network with multi-sensor fusion," in *2018 IEEE International Conference on Multimedia & Expo Workshops (ICMEW)*. IEEE, 2018, pp. 1–5.

[25] J. Kim, S. Lee, and S.-C. Kim, "Modulation type classification of interference signals in automotive radar systems," *IET Radar, Sonar & Navigation*, vol. 13, no. 6, pp. 944–952, 2019.

[26] I. Bilik, S. Villeval, D. Brodeski, H. Ringel, O. Longman, P. Goswami, C. Y. Kumar, S. Rao, P. Swami, A. Jain *et al.*, "Automotive multi-mode cascaded radar data processing embedded system," in *2018 IEEE Radar Conference (RadarConf18)*. IEEE, 2018, pp. 0372–0376.

[27] R. B. GmbH, "Chassis systems control mid-range radar sensor (mrr) for front and rear applications," in *Robert Bosch GmbH*, 2015, pp. 1–4.

[28] S. Lee, B.-H. Lee, J.-E. Lee, and S.-C. Kim, "Statistical characteristic-based road structure recognition in automotive fmcw radar systems," *IEEE Transactions on Intelligent Transportation Systems*, vol. 20, no. 7, pp. 2418–2429, 2018.

[29] S. Lee, Y.-J. Yoon, J.-E. Lee, and S.-C. Kim, "Human–vehicle classification using feature-based svm in 77-ghz automotive fmcw radar," *IET Radar, Sonar & Navigation*, vol. 11, no. 10, pp. 1589–1596, 2017.

[30] B. E. Boser, I. M. Guyon, and V. N. Vapnik, "A training algorithm for optimal margin classifiers," in *Proceedings of the fifth annual workshop on Computational learning theory*, 1992, pp. 144–152.

[31] C.-J. Hsieh, K.-W. Chang, C.-J. Lin, S. S. Keerthi, and S. Sundararajan, "A dual coordinate descent method for large-scale linear svm," in *Proceedings of the 25th international conference on Machine learning*, 2008, pp. 408–415.

[32] C.-W. Hsu and C.-J. Lin, "A comparison of methods for multiclass support vector machines," *IEEE transactions on Neural Networks*, vol. 13, no. 2, pp. 415–425, 2002.

[33] I. W. Tsang, J. T. Kwok, P.-M. Cheung, and N. Cristianini, "Core vector machines: Fast svm training on very large data sets." *Journal of Machine Learning Research*, vol. 6, no. 4, 2005.

[34] Y. Chauvin and D. E. Rumelhart, *Backpropagation: theory, architectures, and applications*. Psychology press, 2013.

[35] N. R. Babu and B. J. Mohan, "Fault classification in power systems using emd and svm," *Ain Shams Engineering Journal*, vol. 8, no. 2, pp. 103–111, 2017.

[36] S. R. Safavian and D. Landgrebe, "A survey of decision tree classifier methodology," *IEEE transactions on systems, man, and cybernetics*, vol. 21, no. 3, pp. 660–674, 1991.

[37] A. Krizhevsky, I. Sutskever, and G. E. Hinton, "Imagenet classification with deep convolutional neural networks," *Advances in neural information processing systems*, vol. 25, 2012.

[38] S. Ioffe and C. Szegedy, "Batch normalization: Accelerating deep network training by reducing internal covariate shift," in *International conference on machine learning*. PMLR, 2015, pp. 448–456.

[39] V. Nair and G. E. Hinton, "Rectified linear units improve restricted boltzmann machines," in *Icml*, 2010.

[40] A. Giusti, D. C. Cireşan, J. Masci, L. M. Gambardella, and J. Schmidhuber, "Fast image scanning with deep max-pooling convolutional neural networks," in *2013 IEEE International Conference on Image Processing*. IEEE, 2013, pp. 4034–4038.

[41] N. Srivastava, G. Hinton, A. Krizhevsky, I. Sutskever, and R. Salakhutdinov, "Dropout: a simple way to prevent neural networks from overfitting," *The journal of machine learning research*, vol. 15, no. 1, pp. 1929–1958, 2014.

[42] S. Ruder, "An overview of gradient descent optimization algorithms," *arXiv preprint arXiv:1609.04747*, 2016.

[43] A. Continental, "408-21 premium long range radar sensor 77 ghz," Technical report, Tech. Rep., 2017.

[44] L. Van der Maaten and G. Hinton, "Visualizing data using t-sne." *Journal of machine learning research*, vol. 9, no. 11, 2008.

[45] M. Toth, P. Meissner, A. Melzer, and K. Witrisal, "Performance comparison of mutual automotive radar interference mitigation algorithms," in *2019 IEEE Radar Conference (RadarConf)*.   IEEE, 2019, pp. 1–6.

[46] J. Choi, "Interference mitigation scheme for automotive fmcw radar," Ph.D. dissertation, The Graduate School of Seoul National University, 2016.

[47] M. Wagner, F. Sulejmani, A. Melzer, P. Meissner, and M. Huemer, "Threshold-free interference cancellation method for automotive fmcw radar systems," in *2018 IEEE International Symposium on Circuits and Systems (ISCAS)*.   IEEE, 2018, pp. 1–4.

[48] J. Bechter, F. Roos, M. Rahman, and C. Waldschmidt, "Automotive radar interference mitigation using a sparse sampling approach," in *2017 European Radar Conference (EURAD)*.   IEEE, 2017, pp. 90–93.

[49] H. Rohling, "Radar cfar thresholding in clutter and multiple target situations," *IEEE transactions on aerospace and electronic systems*, no. 4, pp. 608–621, 1983.

[50] J. An and S. Cho, "Variational autoencoder based anomaly detection using reconstruction probability," *Special Lecture on IE*, vol. 2, no. 1, pp. 1–18, 2015.

[51] P. Vincent, H. Larochelle, Y. Bengio, and P.-A. Manzagol, "Extracting and composing robust features with denoising autoencoders," in *Proceedings of the 25th international conference on Machine learning*, 2008, pp. 1096–1103.

[52] P. Vincent, H. Larochelle, I. Lajoie, Y. Bengio, P.-A. Manzagol, and L. Bottou, "Stacked denoising autoencoders: Learning useful representations in a deep network with a local denoising criterion." *Journal of machine learning research*, vol. 11, no. 12, 2010.

초 록

안정적인 자율 주행을 위해서 주변 환경 인지는 아주 중요하다. 차량의 주행 환경을 정확하게 인지하기 위해 다양한 센서들이 사용되고 있는데, 그 중 레이더 센서는 단가가 낮고, 사용 환경에 영향을 덜 받는다는 장점이 있다. 이러한 이유로 자율 주행을 보조하기 위한 다양한 신호처리 기법이 연구되어 왔고, 일부 기능은 칩으로 구현되어 현재 차량에 부착되어 동작하고 있다.

레이더간 간섭 현상은 두 레이더의 동작 주파수가 겹치면 발생할 수 있다. 간섭 신호는 다른 물체에 반사되지 않고 직접 경로로 수신될 수 있어 그 세기가 클 수 있다. 또한 주파수 응답에서 노이즈 레벨을 증가시키거나 존재하지 않는 고스트 타깃을 생성할 수 있어 탐지율을 낮추고 오경보율을 높이게 된다. 이러한 문제는 레이더 센서가 장착된 자율 주행 차량이 많아진다면 더욱 심각해질 수 있다. 따라서 본 학위 논문에서는 FMCW 레이더를 사용하는 차량용 레이더 시스템에서 발생하는 간섭 신호를 제어하는 기법을 제안한다.

먼저 수신된 신호에 간섭 신호가 존재하는지 파악하는 기법을 제안한다. 간섭 신호가 수신되면 고스트 타깃이 발생할 수 있기 때문에 처리하는 신호에 간섭 신호가 함께 수신되었는지 파악해야한다. 또한 수신되는 간섭 신호의 변조 기법을 알아내는 기법을 제안한다. 먼저 시간 영역 신호에서 특징들을 추출하고 SVM 모델을 활용하여 간섭 신호의 존재 유무와 변조 기법을 파악하였다. 또한 주파수 영역 신호를 입력으로 하는 CNN 모델을 활용하는 연구를 제안한다.

다음으로 수신된 시간 영역 신호 중 간섭 신호가 수신된 구간을 파악하는 기법을 제안한다. 수신된 강한 간섭 신호를 제거하기 이전에 간섭 신호가 수신된 시간 샘플을 찾아야한다. CNN 모델을 활용하여 간섭 구간을 탐지하였고, 기존에 제안된

기법보다 성능이 높음을 확인하였다.

마지막으로 탐지된 간섭 구간의 신호를 타깃 신호로 복원하는 기법을 제안한다. 탐지된 간섭 신호는 0으로 치환되거나 새롭게 복원되는데, 잘못 생성되면 주파수 성분에 원치 않는 성분을 생성하게 된다. 이를 해결하기 위해 수신 신호의 위상을 보정하여 신호 1차적인 근사를 진행하였다. 이 이후에 수신 신호의 도플러 주파수를 이용하여 더 정교한 복원을 진행하였다. 시뮬레이션 데이터와 실측 데이터를 사용하여 제안한 기법이 잔여 주파수 성분을 남기지 않으면서 간섭 신호를 효과적으로 낮추는 것을 확인하였다.